

# Proton-transfer spectroscopy beyond the normal-mode scenario

Florian N. Brüning,<sup>1</sup> Paul Hillmann,<sup>1</sup> Won Kyu Kim,<sup>2</sup> Jan O. Daldrop,<sup>1</sup> and Roland R. Netz<sup>1,\*</sup>

<sup>1</sup>*Freie Universität Berlin, Department of Physics, 14195 Berlin, Germany*

<sup>2</sup>*Korea Institute for Advanced Study, School of Computational Sciences, Seoul 02455, Republic of Korea*

(Dated: July 29, 2022)

A stochastic theory is developed to predict the spectral signature of proton transfer processes and applied to infrared spectra computed from ab initio molecular-dynamics simulations of a single  $\text{H}_5\text{O}_2^+$  cation. By constraining the oxygen atoms to a fixed distance, this system serves as a tunable model for general proton-transfer processes with variable barrier height. Three spectral contributions at distinct frequencies are identified and analytically predicted: the quasi-harmonic motion around the most probable configuration, amenable to normal-mode analysis, the contribution due to transfer paths when the proton moves over the barrier and a shoulder for low frequencies stemming from the stochastic transfer-waiting-time distribution; the latter two contributions are not captured by normal-mode analysis but exclusively report on the proton-transfer kinetics. In accordance with reaction kinetic theory, the transfer-waiting-contribution frequency depends inverse exponentially on the barrier height, whereas the transfer-path-contribution frequency is rather insensitive to the barrier height.

## I. INTRODUCTION

The transfer dynamics of excess protons in the aqueous environment is central to many biochemical processes [1], but despite substantial work, even for acidic water a complete kinetic model that would describe all spectral features encompassing the low THz and infrared (IR) regimes remains elusive. Typically, the discussion is based on two idealized proton-transfer intermediates, namely the  $\text{H}_5\text{O}_2^+$  Zundel cation, where two water molecules symmetrically point their oxygens to the excess proton [2], and the Eigen cation, where hydronium  $\text{H}_3\text{O}^+$  is formed and solvated by three water molecules [3]. Accordingly, proton diffusion in water is portrayed as a stochastic succession of these two states, where the excess proton switches during diffusion: It is a defect that diffuses, rather than a specific proton, which explains the high proton mobility in water [4, 5].

An intensely debated question concerns the relative stability and abundance of the Eigen and Zundel forms in acidic water [6–10]. Several experimental 2D IR studies suggested the Zundel form to dominate the proton-transfer spectroscopic signature in bulk water [8, 9, 11–14]. From ab initio molecular-dynamics (AIMD) work it was concluded that an excess proton in bulk liquid water is predominantly present in the Eigen state and that the Zundel form plays the role of a relatively short-lived transfer or barrier state [15–17]. As the separation between the two water oxygen atoms that flank the excess proton decreases, the relative stability changes and the Zundel form becomes eventually preferred over the Eigen form [18], it transpires that excess proton and water motion are dynamically coupled. As a consequence, proton transfer from one water molecule to a neighboring one not only involves motion of the proton but also of the flanking wa-

ter molecules and even further water neighbors, making the kinetics highly collective [7, 10, 13, 14, 16, 19–23].

In isolated  $\text{H}_5\text{O}_2^+$  clusters and protonated water wires the situation is different from bulk: Experimental [8, 24–27] and theoretical [19, 20, 28–33] work demonstrated that the oxygen-oxygen distance is decreased and the Zundel form is more stable than the hydronium form. By chemical modifications of two proton acceptors in gas-phase clusters, proton-transfer energy barriers of variable heights could be demonstrated [34]. Proton-transfer barriers also exist inside proteins, where amino-acid side chains that act as proton donors can be located at variable separations [35–38]. Thus, energetic barriers for proton transfer exist in a variety of systems and produce characteristic spectroscopic signatures that fundamentally go beyond the established normal-mode picture, as we show in this paper.

The excess proton has a high net charge and during a transfer event covers significant distances over short times, consequently, IR linear and non-linear spectroscopy are very suitable methods to detect proton-transfer events and have been applied to bulk acidic solutions [2], acidic water clusters [24], gas-phase ions [39] and proteins [40]. Interpretation of experimental spectra is traditionally based on normal-mode analysis around one or multiple local energy minima, where the normal-mode frequency  $f_{\text{NM}}$  defines a vibrational time scale according to  $\tau_{\text{NM}} = 1/f_{\text{NM}}$ . But if a barrier exists, two additional time scales emerge, the transfer-waiting time  $\tau_{\text{TW}}$ , which is the time the proton waits in one minimum before it transfers [41–43], and the transfer-path (TP) time  $\tau_{\text{TP}}$ , which is the time the actual transfer over the barrier takes [44–48].

In this paper, we show by a combination of stochastic theory and ab initio molecular-dynamics (AIMD) simulations, that the normal-mode, the transfer-waiting and the TP time scales, which together characterize the transfer-waiting kinetics, leave distinct and characteristic spectroscopic traces. As a specific example, we consider a  $\text{H}_5\text{O}_2^+$  cation in gas phase. In order to probe dif-

\* rnetz@physik.fu-berlin.de

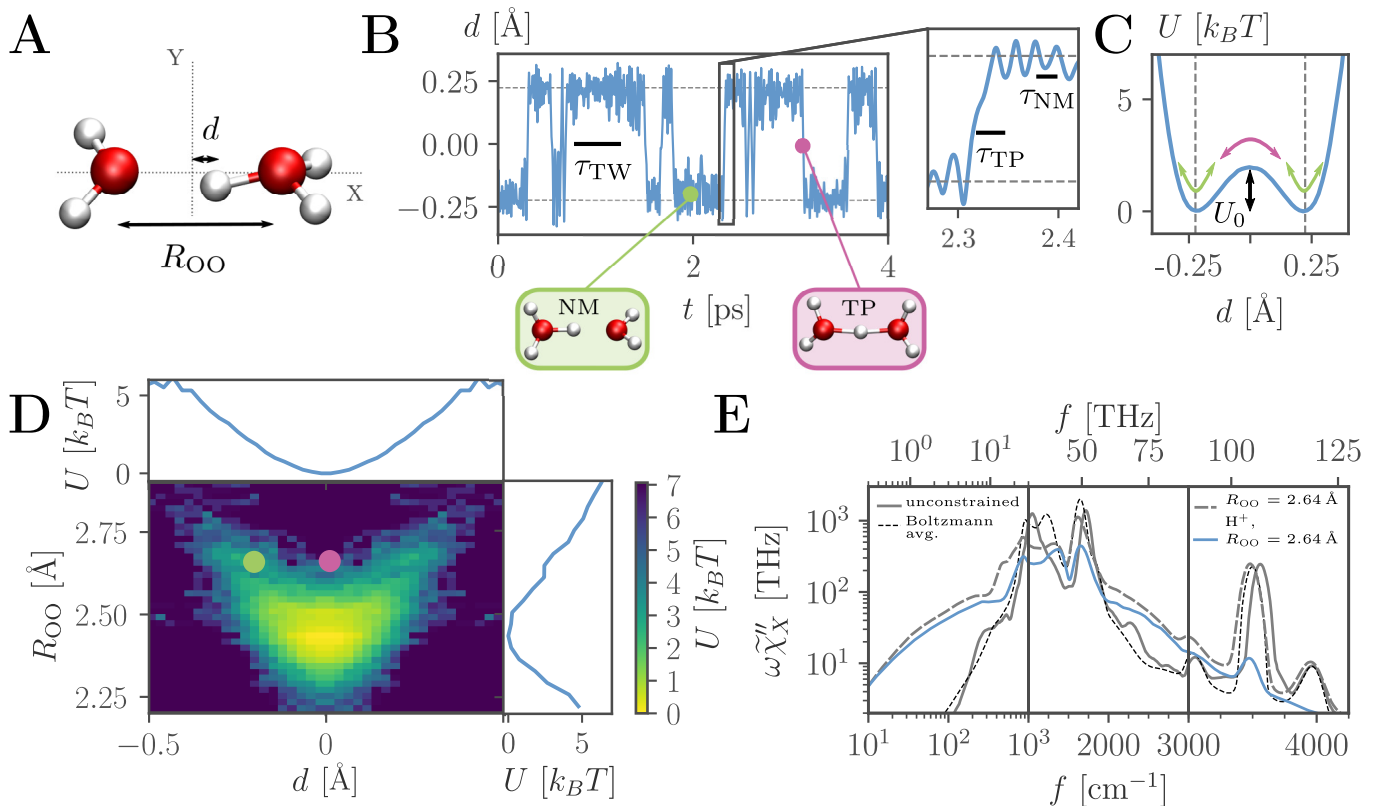


Figure 1. Ab initio molecular-dynamics (AIMD) simulations of the  $\text{H}_5\text{O}_2^+$  cation. **A** The oxygen-oxygen separation  $R_{\text{OO}}$  and the proton distance from the oxygen midpoint along the  $x$  axis, named  $d$ , describe the excess-proton dynamics. **B** The excess proton trajectory for fixed  $R_{\text{OO}} = 2.64 \text{ \AA}$  visualizes the transfer-waiting time  $\tau_{\text{TW}}$  as well as the normal-mode time  $\tau_{\text{NM}}$  and the transfer-path (TP) time  $\tau_{\text{TP}}$  (see inset). Selected snapshots show structures at the free-energy minimum and at the barrier top. **C** Free-energy profile for fixed  $R_{\text{OO}} = 2.64 \text{ \AA}$ , extracted from constrained simulations. **D** 2D free-energy landscape in terms of  $R_{\text{OO}}$  and  $d$  from unconstrained simulations. **E** Absorption spectra along the  $x$  axis where  $\omega = 2\pi f$ . The grey solid line shows the total (i.e. nuclear + electronic) spectrum of the unconstrained system, compared with the Boltzmann average of constrained systems (black broken line). The grey broken line shows the total spectrum for constrained  $R_{\text{OO}} = 2.64 \text{ \AA}$ , compared to the spectrum of only the excess proton (blue line, multiplied by a factor of 2). Note the change of scales at  $f = 1000 \text{ cm}^{-1}$  and  $f = 3000 \text{ cm}^{-1}$ .

ferent proton-transfer barrier heights, we constrain the separation between the two water oxygen atoms at variable fixed distances, applicable to proteins and other systems where proton accepting residues are positioned at well-defined distances [35–37]. While the transfer-waiting time depends exponentially on the barrier height  $U_0$  as  $\tau_{\text{TW}} \sim e^{U_0/k_B T}$  [41, 43], the normal-mode time scale  $\tau_{\text{NM}}$  is determined by the stiffness of the effective harmonic potential  $k$  and the effective mass  $m$  according to  $\tau_{\text{NM}} = 2\pi\sqrt{m/k} \sim 1/\sqrt{U_0}$ , and the TP time depends logarithmically on  $U_0$  as  $\tau_{\text{TP}} \sim \ln(U_0/k_B T)/U_0$  [46–48]. From the different functional dependencies on  $U_0$ , one expects for not too low barrier heights  $\tau_{\text{NM}} \sim \tau_{\text{TP}} < \tau_{\text{TW}}$ . Indeed, for an oxygen-oxygen distance of  $R_{\text{OO}} = 2.64 \text{ \AA}$ , which in our AIMD simulations of the  $\text{H}_5\text{O}_2^+$  cation leads to a moderate effective barrier height of  $U_0 = 2.0 k_B T$ , the normal-mode spectroscopic contributions lie between  $1000 \text{ cm}^{-1}$  to  $2000 \text{ cm}^{-1}$ , the TP contribution turns out to be a rather well defined band centered around  $800 \text{ cm}^{-1}$ ,

and since the waiting-time distribution is rather broad, the transfer-waiting contribution forms a continuum band below  $500 \text{ cm}^{-1}$  that reaches deep into the GHz range, in agreement with experimental THz absorption measurements [49, 50].

Our AIMD results show that the broad low-frequency transfer-waiting spectral contribution crucially depends on the barrier height, controlled by the relative distance of the water molecules sharing the excess proton. In contrast, the TP spectral contribution shifts only slightly with barrier height, in agreement with transfer kinetic theory [46–48]. Isotope exchange of the excess proton on the other hand affects the TP contribution but not the waiting-time contribution, as we predict by stochastic theory. In summary, we show that the spectroscopic signature of proton barrier crossing reflects transfer-waiting statistics as well as TP kinetics and in particular cannot be modeled by a succession of normal modes located across the barrier. Our results also apply to experimental

systems with fluctuating barrier heights, such as acidic water, as recently considered by a combined theoretical/experimental study [50]: We show that the spectrum of unconstrained  $\text{H}_5\text{O}_2^+$  can be quite accurately reproduced by Boltzmann averaging of spectra of constrained systems, thus all features we see in our constrained simulations are also expected in experimental systems where the proton acceptor separation can fluctuate. Quantum zero-point-motion effects reduce the effective barrier height [10, 15, 16, 28, 51], but for large enough barrier heights are not expected to eliminate the spectroscopic features we predict, as discussed in SI section I.

## II. RESULTS AND DISCUSSION

We perform AIMD simulations of a single  $\text{H}_5\text{O}_2^+$  cation with a total trajectory length of 5 ns for several constrained oxygen separations as well as for unconstrained oxygens (see Methods for details). Suitable reaction coordinates are the oxygen-oxygen distance  $R_{\text{OO}}$  and the excess-proton distance from the oxygen mid-point position,  $d = \frac{1}{2}(R_{\text{O}_1\text{H}} - R_{\text{O}_2\text{H}})_x$ , projected onto the x-axis that connects the two oxygens, as illustrated in fig. 1A. The two-dimensional free energy in fig. 1D, calculated from the probability distribution of unconstrained simulations according to  $U(R_{\text{OO}}, d) = -k_B T \ln p(R_{\text{OO}}, d)$ , demonstrates that the global minimum of the free energy is located around  $R_{\text{OO}} = 2.40 \text{ \AA}$  and  $d = 0$ . This is the symmetric Zundel state, where the excess proton is symmetrically shared by the oxygens [2]. For  $R_{\text{OO}} > 2.55 \text{ \AA}$  a double-well free-energy landscape along  $d$  appears, which indicates a preferred localization of the excess proton near one water molecule, analogous to the Eigen state in bulk water [3]. The excess proton trajectory for constrained  $R_{\text{OO}} = 2.64 \text{ \AA}$  in fig. 1B is typical for the thermally activated barrier crossing of a weakly damped massive particle [43] and involves a moderate barrier height of  $U_0 = 2.0 k_B T$ , as seen in the corresponding free-energy profile in fig. 1C. Most of the time the excess proton is part of a  $\text{H}_3\text{O}^+$  molecule and vibrates in one of the two free-energy minima with an oscillation time described by the normal-mode time  $\tau_{\text{NM}} = 17 \text{ fs}$  (inset fig. 1B), while from time to time the proton suddenly crosses the barrier, the mean time of such a TP is  $\tau_{\text{TP}} = 25 \text{ fs}$  (inset fig. 1B). The longest time scale is the transfer-waiting time, which for  $R_{\text{OO}} = 2.64 \text{ \AA}$  is  $\tau_{\text{TW}} = 440 \text{ fs}$ . In fig. 1E we show as a grey solid line the absorption spectrum of the unconstrained  $\text{H}_5\text{O}_2^+$  cation along  $x$ , the oxygen separation direction, calculated from the entire nuclear and electronic polarizations (see Methods). It shows in addition to the OH stretch and HOH bend bands at  $3400 \text{ cm}^{-1}$  and  $1800 \text{ cm}^{-1}$ , respectively, a prominent feature at  $1000 \text{ cm}^{-1}$ , which is the Zundel normal mode, where the excess proton vibrates in a rather soft potential produced by the two flanking water molecules (see SI section II and III for a literature overview). The spectrum for the constrained system with  $R_{\text{OO}} = 2.64 \text{ \AA}$ , grey broken line,

displays a band at  $800 \text{ cm}^{-1}$  and a very broad shoulder that extends down to the lowest frequencies. As we show in this paper, these two spectral features stem from proton TPs and proton transfer-waiting-time stochastics, respectively, and are the only spectroscopic contributions that reflect the actual proton-transfer kinetics. Interestingly, the spectral contribution of only the excess proton for fixed  $R_{\text{OO}} = 2.64 \text{ \AA}$  (blue solid line, multiplied by a factor of 2) is almost identical to the full spectrum (grey line), so we conclude that the IR spectrum is predominantly caused by proton motion and can thus be used to investigate excess-proton dynamics (more details are given in SI section IV). In fact, the spectrum of the unconstrained system (black broken line) agrees well with the free-energy-weighted Boltzmann average over constrained spectra with different  $R_{\text{OO}}$  values (black dashed line, see SI section V for details), indicating that the proton and the oxygen dynamics decouple. Our simulation model with constrained oxygen-oxygen separation thus is also a tool to decompose and thereby understand unconstrained system dynamics (a finding that is obvious only for static observables [52]).

In order to distinguish transfer-waiting, TP and normal-mode spectral contributions, the proton trajectory  $d(t)$  is decomposed according to  $d(t) = d_{\text{TW}}(t) + d_{\text{TP}}(t) + d_{\text{NM}}(t)$ , as illustrated in fig. 2A for  $R_{\text{OO}} = 2.64 \text{ \AA}$ . The transfer-waiting part  $d_{\text{TW}}(t)$  describes two-state kinetics with instantaneous transfers when the trajectory last crosses a free-energy minimum at  $d_{\text{TW}}^* = \pm 0.22 \text{ \AA}$ . The TP contribution  $d_{\text{TP}}(t)$  consists of transfer trajectories between last and first crossing the free-energy minima, including recrossings where the proton shuttles repeatedly back and forth between the minima. Recrossings are rather frequent for the low friction experienced by the proton [43] (see SI section VI), a three-fold recrossing event is seen in the proton trajectory in fig. 2A at  $t = 0.6 \text{ ps}$ . Finally, the normal-mode part  $d_{\text{NM}}(t)$  comprises the trajectory remainder.

Fig. 2B shows in blue the simulated excess-proton spectrum decomposed into its three components according to  $\tilde{\chi}'' = \tilde{\chi}''_{\text{B}} + \tilde{\chi}''_{\text{TP}} + \tilde{\chi}''_{\text{NM}}$ , the red broken lines show theoretical predictions (which will be explained further below). Trajectory decomposition in the time domain creates spectral cross contributions, which are relatively small, as shown in SI sections VII and VIII, and are added to  $\tilde{\chi}''_{\text{NM}}$ . The transfer-waiting spectrum  $\tilde{\chi}''_{\text{TW}}$  in fig. 2B2 displays a pronounced low-frequency shoulder, which reflects the transfer-waiting-time distribution. The TP spectrum  $\tilde{\chi}''_{\text{TP}}$  in fig. 2B3 is a rather well defined band at  $800 \text{ cm}^{-1}$ . Even though the time fraction the excess proton spends on TPs is only 16% for  $R_{\text{OO}} = 2.64 \text{ \AA}$ , the spectral contribution is significant due to the large and quick charge displacement: The proton transfer velocity of roughly  $v_{\text{TP}} = 2d_{\text{TP}}^*/\tau_{\text{TP}} = 0.44 \text{ \AA}/25 \text{ fs} = 1.8 \times 10^3 \text{ m/s}$  is slightly larger than the proton thermal velocity of  $v_{\text{th}} = \sqrt{k_B T/m_p} = 1.5 \times 10^3 \text{ m/s}$ , where  $m_p = 1.7 \times 10^{-27} \text{ kg}$  is the proton mass. This confirms previous findings that TPs correspond to the high-energetic part of the Maxwell-

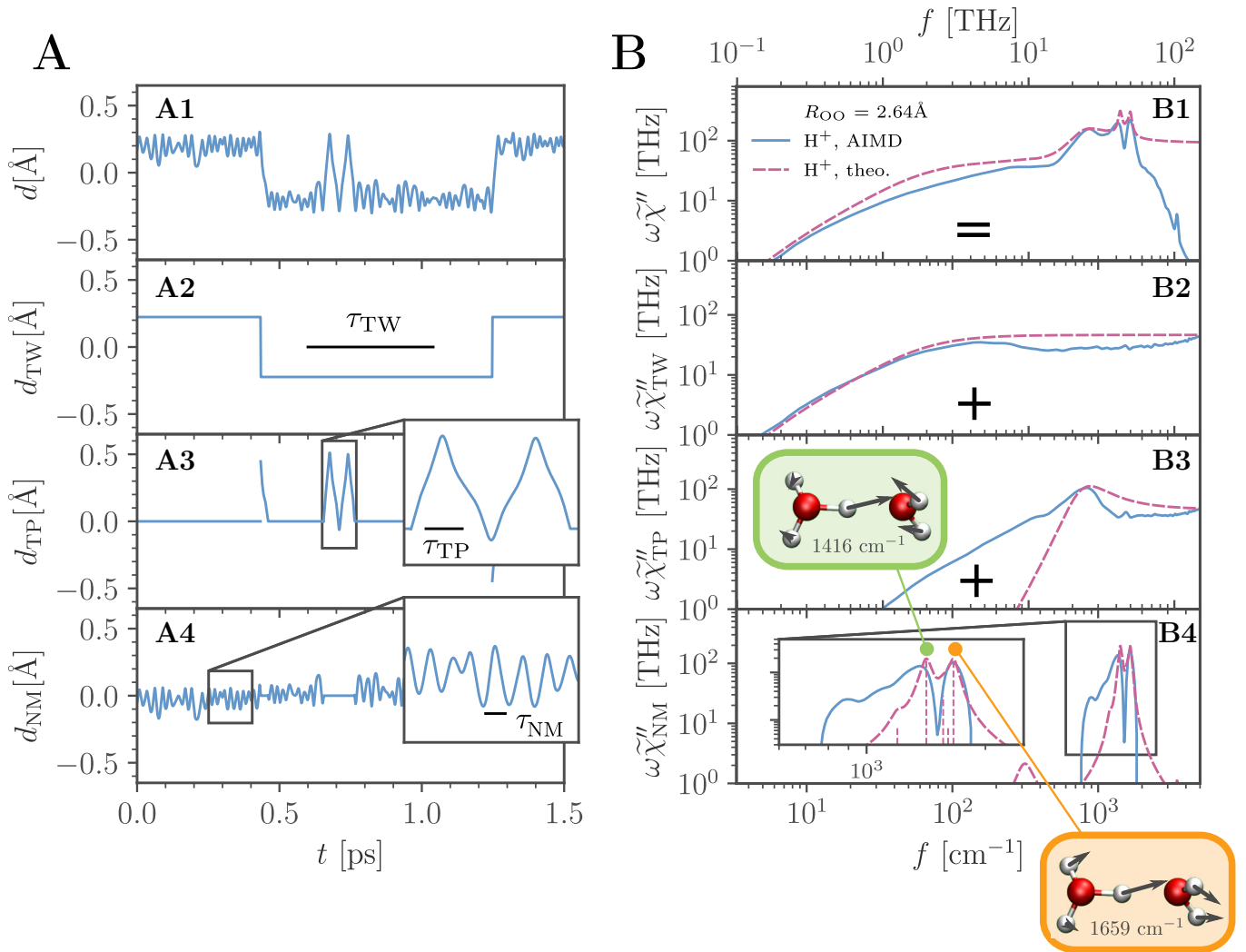


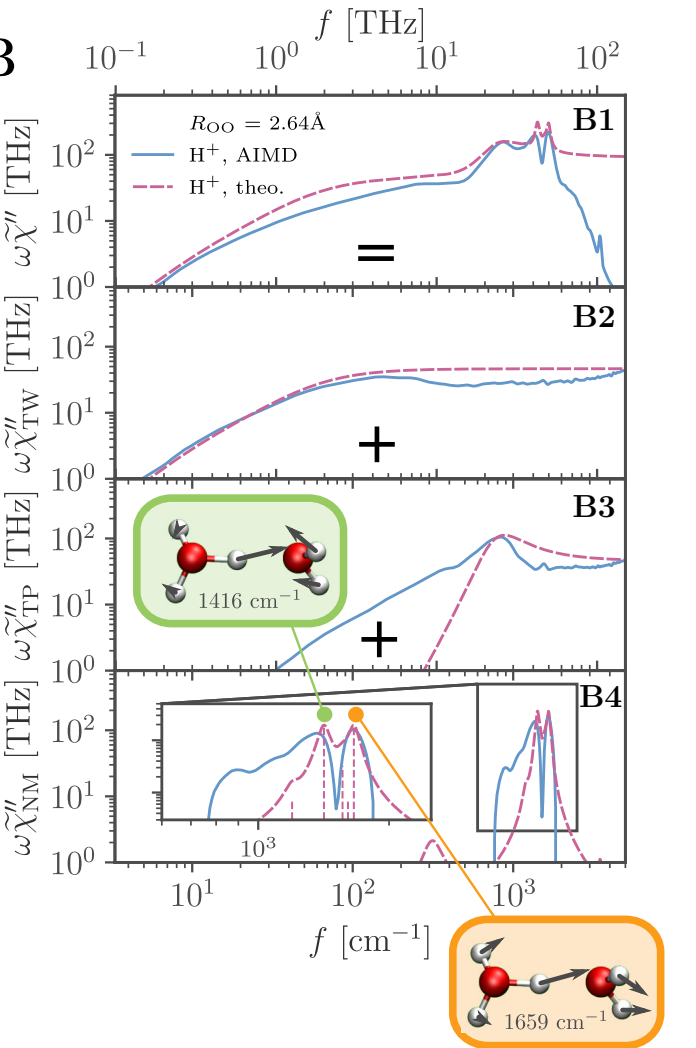
Figure 2. AIMD simulations of a  $\text{H}_5\text{O}_2^+$  cation with constrained  $R_{\text{OO}} = 2.64 \text{ \AA}$ . **A** Decomposition of the excess-proton trajectory  $d(t)$  into the two-state transfer-waiting contribution  $d_{\text{TW}}(t)$ , the TP contribution  $d_{\text{TP}}(t)$  and the remaining normal-mode contribution  $d_{\text{NM}}(t)$ . **B** Blue solid lines show the simulated excess-proton spectrum  $\omega\tilde{\chi}''$  and its decomposition into the transfer-waiting  $\omega\tilde{\chi}''_{\text{TW}}$ , the TP  $\omega\tilde{\chi}''_{\text{TP}}$  and the normal-mode contribution  $\omega\tilde{\chi}''_{\text{NM}}$ . The red broken lines in B2 and B3 show the corresponding theoretical predictions according to eqs. (1) and (5). The red broken line in B4 shows the normal-mode spectrum including friction-induced line broadening. The snapshots illustrate the two dominant normal modes at  $1416 \text{ cm}^{-1}$  and  $1659 \text{ cm}^{-1}$ .

Boltzmann ensemble, i.e. the excess proton initiates a TP only when its kinetic energy is above average [53]. The normal-mode spectrum  $\tilde{\chi}''_{\text{NM}}$  in fig. 2B4 consists of two main peaks.

We will now present analytic theories for each simulated spectral contribution shown in figs. 2B2–B4. A stochastic two-state process has the spectrum

$$\omega\tilde{\chi}''_{\text{TW}}(\omega) = \frac{2q^2 d_{\text{TW}}^{*2}}{V\epsilon_0 k_B T} \text{Re} \left( \frac{\omega^2 \tilde{q}_{\text{TW}}(\omega)}{1 - \tilde{p}_{\text{TW}}(\omega)^2} \right) \quad (1)$$

and depends on the Fourier-transformed transfer-waiting-time distribution  $\tilde{p}_{\text{TW}}(\omega)$  and the survival distribution  $\tilde{q}_{\text{TW}}(\omega)$ , which is defined as  $q_{\text{TW}}(t) = \int_t^\infty p_{\text{TW}}(t') dt'$ , the positions of the free-energy minima  $\pm d_{\text{TW}}^*$ , the excess proton charge  $q = e$  and the system volume  $V$  (see SI



Sect. IX for a detailed derivation). Using  $d_{\text{TW}}^* = 0.22 \text{ \AA}$  and bi-exponential fits for  $p_{\text{TW}}(t)$  to the simulation data in fig. 4C,  $\omega\tilde{\chi}''_{\text{TW}}(\omega)$  according to eq. (1) (red broken line) matches the simulation data (blue solid line) in fig. 2B2 very well without any fitting parameters. For a single-exponential waiting-time distribution,  $p_{\text{TW}}(t) = \tau_{\text{TW}}^{-1} \exp(-t/\tau_{\text{TW}})$ , eq. (1) simplifies to

$$\omega\tilde{\chi}''_{\text{TW}}(\omega) = \frac{2q^2 d_{\text{TW}}^{*2}}{V\epsilon_0 k_B T} \frac{\tau_{\text{TW}} \omega^2}{(4 + \tau_{\text{TW}}^2 \omega^2)}, \quad (2)$$

which shows that the spectrum is identical to an overdamped harmonic oscillator with a corner frequency  $\omega_{\text{TW}}^* \sim 1/\tau_{\text{TW}}$  (see SI section X for details). For large frequencies  $\omega\tilde{\chi}''_{\text{TW}}$  is constant and proportional to the

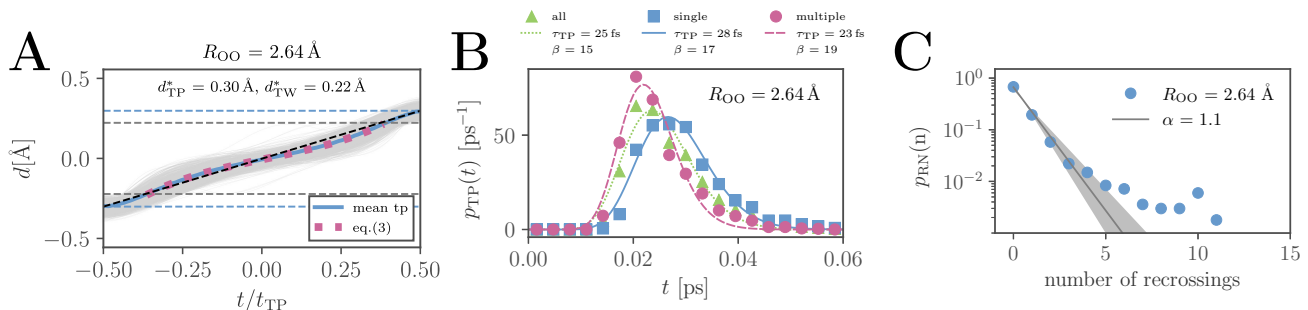


Figure 3. TP statistics. **A** Ensemble of all 2829 proton TPs for constrained  $R_{OO} = 2.64 \text{ \AA}$  (grey lines) as a function of the rescaled time  $t/t_{TP}$ , where  $t_{TP}$  is the individual TP time. Horizontal blue dashed lines indicate the mean TP terminal positions  $\pm d_{TP}^*/2$ , defined by the TP turning points, while horizontal grey dashed lines indicate the free-energy minima  $\pm d_{TW}^*/2$ . The simulated mean TP (blue line) agrees well with the path-integral prediction eq. (3) (red dotted line). The straight black dashed line approximates the TP shape also quite well. **B** Distribution  $p_{TP}$  of all TPs (green triangles) and a decomposition into single (non-recrossing, blue squares) and multiple (recrossing, red dots) TPs together with fits according to eq. (4). **C** Recrossing-number probability distribution  $p_{RN}(n)$  compared to an exponential fit  $p_{RN}(n) = (1 - e^{-\alpha})e^{-\alpha n}$ , the confidence interval  $\alpha \pm 20\%$  is shown by grey lines.

transfer-waiting rate,  $\omega \tilde{\chi}_{TW}'' \sim 1/\tau_{TW}$ , for small frequencies  $\omega \tilde{\chi}_{TW}'' \sim \tau_{TW} \omega^2$ .

The TP spectral contribution depends on the TP shape. The ensemble of all 2829 TPs observed in the simulations for  $R_{OO} = 2.64 \text{ \AA}$  is shown in fig. 3A (grey lines), together with the mean TP (blue solid line) obtained by position averaging. The path-integral saddle-point prediction for the TP shape over a parabolic barrier [48],

$$d_{TP}(t) = d_{TW}^* \left[ e^{t/\kappa} - e^{-t/\kappa} \right] / \mathcal{N}, \quad (3)$$

(red dotted line) matches the simulated mean TP shape very well ( $\mathcal{N}$  is a normalization constant). In SI section XI it is shown that eq. (3) corresponds to the exact mean TP shape in the high-barrier limit [47]. The fitted characteristic time  $\kappa = d_{TW}^{*2} \gamma / (2U_0) = 6.5 \text{ fs}$  depends on the effective friction coefficient  $\gamma$  acting on the proton as it moves over the barrier. A straight line (black broken line) describes the simulated mean TP shape also quite well. Fig. 3B shows the TP-time distribution of all TPs (green triangles) together with a decomposition into single (non-recrossing, blue squares) and multiple (recrossing, red dots) TPs, where the TP time  $\tau_{TP}$  is defined from the turning points of the TPs. It is seen that multiple TPs that consist of recrossing trajectories are significantly faster than single TPs, which reflects that recrossing protons have a higher kinetic energy and thereby tend to rebound back over the barrier. Fits according to the Erlang distribution [54]

$$p_{TP}(t) = \frac{t^{\beta-1}}{(\beta-1)!} \left( \frac{\beta}{\tau_{TP}} \right)^\beta e^{-\beta t/\tau_{TP}} \quad (4)$$

are shown as lines. In Fig. 3C the simulated recrossing-number distribution  $p_{RN}(n)$  is compared to an exponential fit with a decay constant  $\alpha = 1.1$ , 40 % of all TPs are single transfer events,  $n = 0$ , while the remaining 60 % TPs are part of multiple events with  $n > 0$ .

Combining the TP time distribution  $p_{TP}(t)$  in the infinitely sharp limit  $\beta \rightarrow \infty$ , the exponential recrossing-number distribution  $p_{RN}(n)$  and approximating the TP shape as a straight line, the analytical result for the TP spectral contribution (red broken line in fig. 2B3) is in SI section XII derived as

$$\omega \tilde{\chi}_{TP}''(\omega) = \frac{d_{TP}^{*2} q^2}{V \epsilon_0 k_B T \tau_{TW}} \frac{64 \omega^2 \tau_{TP}^2}{\pi^4 (\omega \tau_{TP} + \pi)^2} \frac{e^\alpha \omega^2 \tau_{TP}^2}{2 \cosh(\alpha) - 2 + (\omega \tau_{TP} - \pi)^2} \quad (5)$$

and matches the simulation data (blue solid line) around the maximum quite well. In the comparison the mean time of recrossing TPs  $\tau_{TP} = 23 \text{ fs}$  from fig. 3B is used, which is shown to be the dominating time scale in SI section XII. Interestingly, the TP spectrum eq. (5) is a product of a Debye and a Lorentzian line shape, both with the same characteristic frequency  $f_{TP} = 1/(2\tau_{TP})$ , which explains its relative sharpness.

The remaining normal-mode contribution  $\tilde{\chi}_{NM}''$  in fig. 2B4 is obtained by harmonic analysis of the minimal energy structure including line broadening from frictional damping (red broken line). The two dominant normal modes around  $1416 \text{ cm}^{-1}$  and  $1659 \text{ cm}^{-1}$ , which correspond to in-phase and out-of-phase coupled vibrations of the excess proton with the hydrogens of the distant water, are illustrated in fig. 2B4 (see Methods and SI section III for details).

In fig. 2B1 the simulated excess-proton spectrum (blue solid line) is compared to the sum of the theoretical transfer-waiting, TP and normal mode predictions (red broken line), the agreement is good (except for very high frequencies), which demonstrates that eqs. (1) and (5) together with the normal-mode analysis allow to quantitatively describe excess-proton transfer spectra.

The excess-proton spectra in fig. 4A1 vary significantly for different values of  $R_{OO}$ . The excess-proton free energies

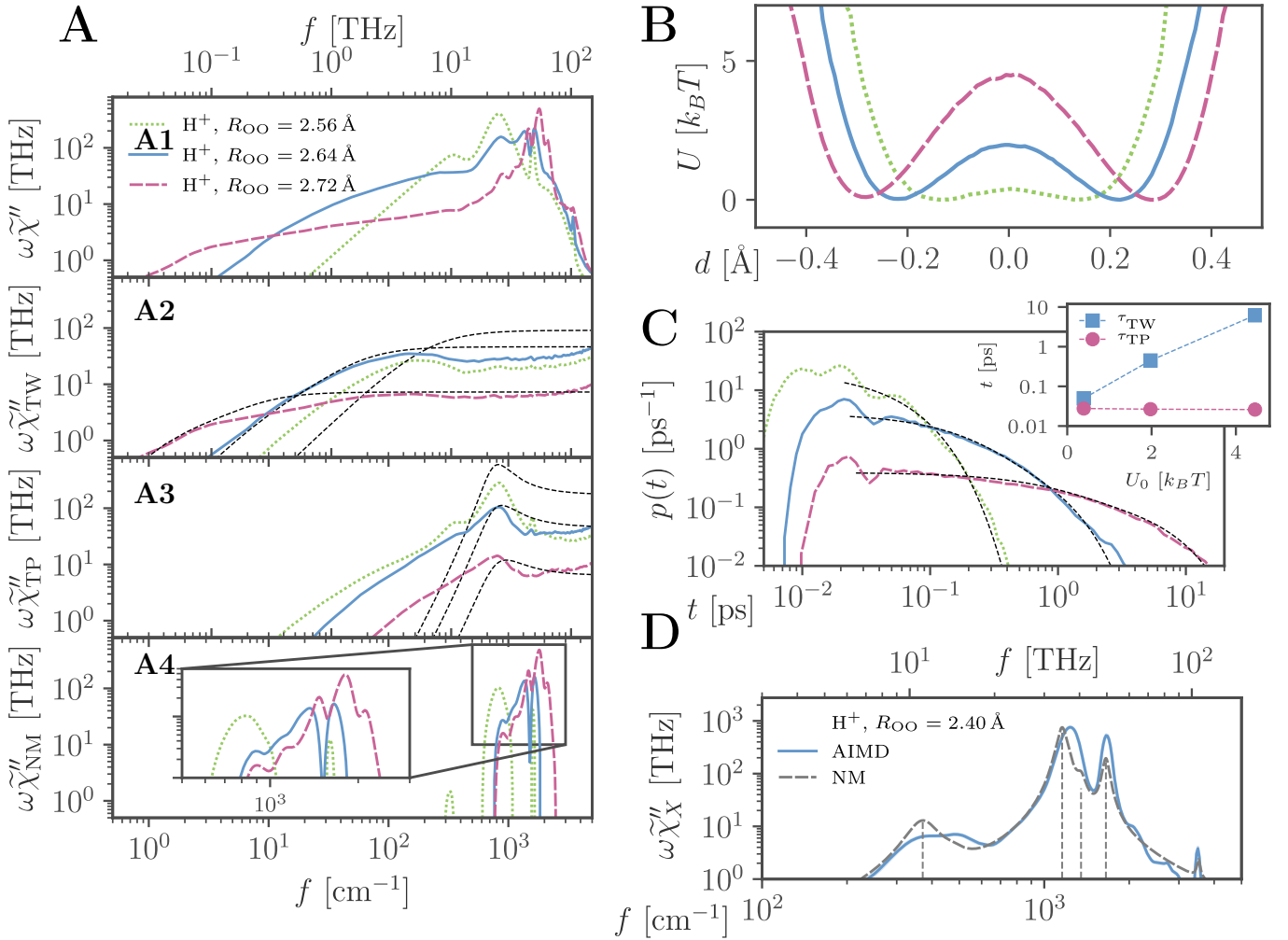


Figure 4. Decomposition of the excess-proton spectra for various constrained  $R_{OO}$ . **A** AIMD spectra are shown as colored lines and theoretical predictions are shown for the transfer-waiting contribution, eq. (1), in A2 and for the TP contribution, eq. (5), in A3 as thin black broken lines. See SI section XIII for details. **B** Proton free energies landscapes extracted from simulation trajectories. **C** Transfer-waiting-time distributions together with bi-exponential fits (black broken lines). The inset shows the mean transfer-waiting times  $\tau_{\text{TW}}$  and the mean TP times  $\tau_{\text{TP}}$  as a function of the free-energy barrier height  $U_0$ . **D** IR spectrum of the excess proton (blue solid line) in the  $\text{H}_5\text{O}_2^+$  cation with fixed  $R_{OO} = 2.40 \text{ \AA}$  compared to the normal-mode spectrum including frictional line-broadening (grey broken line). Vertical grey broken lines denote the dominant normal modes.

from simulations in fig. 4B demonstrate that the three systems exhibit high, moderate and low barriers. Very pronounced is the change of the low-frequency shoulder of the transfer-waiting contribution in fig. 4A2, which moves to lower frequencies and becomes weaker with growing barrier height and is well captured by the theoretical predictions eq. (1) (black broken lines) using bi-exponential fits to the transfer-waiting distributions in fig. 4C. Eq. (2) demonstrates that the spectral differences are due to less frequent transfers as the barrier height increases. The simulated mean transfer-waiting time  $\tau_{\text{TW}}$  in the inset of fig. 4C exponentially increases with the barrier height  $U_0$ , as expected for thermally activated barrier crossing [41, 43]. On the other hand, the frequency of the TP spectral contribution in fig. 4A3 shifts very little for different  $R_{OO}$ , which is well-captured by eq. (5) (black

broken lines) and reflects the weak dependence of the TP time  $\tau_{\text{TP}}$  on the barrier height in the inset of fig. 4C, in agreement with the predicted logarithmic dependence of  $\tau_{\text{TP}}$  on the barrier height [46].

Fig. 4D compares the IR spectrum of the excess proton (blue solid line) in the  $\text{H}_5\text{O}_2^+$  cation to the normal-mode spectrum including frictional line broadening (grey broken line, see SI section III for details) for fixed  $R_{OO} = 2.40 \text{ \AA}$ , the barrier-less global minimum of the unconstrained  $\text{H}_5\text{O}_2^+$  cation. The good agreement highlights that the barrierless Zundel state is well described by a normal-mode analysis. This is in contrast to the results for larger values of  $R_{OO}$  in fig. 4A, where a finite barrier exists and the transfer-waiting and TP spectral signatures dominate over the normal-mode contribution.

### III. CONCLUSIONS AND DISCUSSION

In contrast to traditional normal-mode-based approaches to proton-transfer spectroscopy, which consider proton vibrations around energy minima, we here investigate the spectrum of a proton as it actually makes the move from one energy minimum to another. While the normal-mode frequencies are on the harmonic-approximation level determined by the curvature of the energy landscape and by the effective mass, two fundamentally different time scales govern the barrier-crossing absorption spectrum: the mean time the proton waits in a potential minimum before it crosses the barrier, the transfer-waiting time, and the mean time it takes the proton to actually move over the barrier once it has left the potential minimum, the so-called transfer-path (TP) time. While the TP time distribution is rather narrow, which leads to a well-defined TP band, the transfer-waiting times are broadly distributed, which leads to a wide spectral absorption down to low frequencies. Recent experimental studies on hydrochloric acid solutions in the THz regime indeed observed broad absorption that by comparison with AIMD simulations could be attributed to proton motion [49, 50]. The AIMD simulations of single  $\text{H}_5\text{O}_2^+$  cations reveal a high similarity of excess-proton-only spectra and spectra from all nuclei and electronic polarizations. This emphasizes the impact of proton-transfer processes on experimentally measured spectra and allows in turn to develop a stochastic spectral theory based on excess-proton motion only. The excess-proton transfer between two water molecules depends strongly on the separation of the two water oxygens. For oxygen-oxygen separations  $R_{\text{OO}} \geq 2.5 \text{ \AA}$  a barrier crossing is involved, whereas for closer separations the proton is rather located directly in between the two water molecules.

An H/D isotope exchange of the excess proton does not shift the low-frequency transfer-waiting signature, as shown in SI section XIV, which is expected since the excess-proton barrier crossing is a friction-dominated process and mass plays only a minor role, as discussed in SI section XV. In contrast, TP and normal-mode signatures show isotope effects, which suggests how to experimentally distinguish barrier crossing from the other spectral contributions. For the normal-mode spectral contribution the isotope effect is well known (see section X in the SI), the mass-dependence of the TP spectral contribution is rather subtle and depends on the stochastic mass-friction balance (see section XV in the SI).

The spectroscopic signatures of proton transfer are most pronounced along the transfer direction, as shown in section V in the SI, thus dichroic measurements [33, 38] are most suitable to observe these features.

#### Methods

The Born-Oppenheimer AIMD simulations of the  $\text{H}_5\text{O}_2^+$  cation were performed with the CP2K 4.1 software pack-

age using a doubly polarizable triple-zeta basis set for the valence electrons, dual-space pseudopotentials, the BLYP exchange-correlation functional and D3 dispersion correction [55–57]. The simulation box size was  $10 \times 10 \times 10 \text{ \AA}^3$  and the cutoff for the plane-wave representation 400 Ry. For each constrained system 20 ps simulations with a time step of 0.5 fs were performed under NVT conditions at 300 K by coupling all atoms to a CSV thermostat with a time constant of 100 fs, which has been shown to be exceptionally good for preserving vibrational dynamics [58]. Consequently a number of independent simulations with a time step of 0.25 fs were performed under NVE conditions starting from different snapshots of the NVT data,  $12 \times 20 \text{ ps}$  for the systems with  $R_{\text{OO}} \leq 2.5 \text{ \AA}$  and  $\geq 20 \times 60 \text{ ps}$  for the systems with  $R_{\text{OO}} \geq 2.5 \text{ \AA}$ ,  $20 \times 90 \text{ ps}$  for  $R_{\text{OO}} = 2.72 \text{ \AA}$ . Even though the time step was chosen very small, some systems did not preserve energy during the NVE simulation due to unfavorable starting conditions and the small number of degrees of freedom. These systems were excluded from further analysis. The data of systems with constrained oxygen atoms stem from NVE simulations, totaling in 240 ps to 1800 ps simulation time for each system. In case of the unconstrained system, the oxygen atoms were only constrained in the  $yz$ -plane. Nevertheless the NVE simulations were less stable due to large spatial fluctuations along  $x$ . For this system NVT simulations with a total simulation time of 20 ps were performed.

Linear response theory relates the dielectric susceptibility  $\chi(t)$  to the equilibrium autocorrelation of the dipole moment  $C(t) = \langle \mathbf{p}(t)\mathbf{p}(0) \rangle$ , reading in Fourier space

$$\tilde{\chi}(\omega) = \frac{1}{V\epsilon_0 k_B T} \left( C(0) - i\frac{\omega}{2} \tilde{C}^+(\omega) \right), \quad (6)$$

with system volume  $V$ , thermal energy  $k_B T$  and vacuum permittivity  $\epsilon_0$ . IR spectra can therefore be calculated straight-forwardly from sufficiently sampled trajectories of the AIMD simulation data using eq. (6) and the Wiener-Kintchin relation, derived in SI section XVI. Quantum corrections have previously been addressed [59], but were not applied here. The dipole moments were obtained after Wannier-center localization of the electron density at a time resolution of 2 fs. The power spectra were smoothed using Gaussian kernels with widths that are logarithmically increasing from  $20 \text{ cm}^{-1}$  centered at  $20 \text{ cm}^{-1}$  to  $100 \text{ cm}^{-1}$  centered at  $5000 \text{ cm}^{-1}$ . All presented spectra were scaled by the volume of two water molecules,  $V = 0.060 \text{ nm}^3$ , which follows from the density of water at atmospheric pressure and 300 K,  $\rho = 0.99 \text{ g/ml}$ . The normal-mode analysis was performed using the implementation in CP2K 4.1 by diagonalizing the Hessian of energetically optimal structures for the same system parameters as in the AIMD simulations. The normal modes were obtained as the Eigenvectors of the Hessian, the Eigenvalues are the frequencies. A projection of the Eigenvectors onto the excess-proton coordinate gave their spectral contributions. Line broadening resulted from frictional damping with the same fitted friction coefficient

$\gamma = 16$  u/ps for all normal modes (see SI Sect. X for details).

## SUPPLEMENTARY MATERIAL

See Supplementary Material for detailed derivations, analysis procedures, additional data and discussion

## AUTHOR CONTRIBUTIONS

F.N.B. and R.R.N. conceived the theory and designed the simulations. F.N.B. performed the AIMD simulations and analyzed the data. P.H. performed the quantum-mechanical zero-point calculations. W.K.K. contributed to the transfer-path-shape theory. All authors discussed the results, analyses and interpretations. F.N.B. and

R.R.N. wrote the paper with input from all authors.

## ACKNOWLEDGMENTS

We gratefully acknowledge support by the DFG grant SFB 1078, project C1 and computing time on the HPC clusters at the physics department and ZEDAT, FU Berlin. W.K.K. acknowledges the support by a KIAS Individual Grant (CG076001) at Korea Institute for Advanced Study.

## COMPETING INTERESTS

The authors declare no competing interests.

## DATA AVAILABILITY STATEMENT

The data that support the findings of this study are available from the corresponding author upon request.

- 
- [1] Marx, D. Proton transfer 200 years after Von Grothuss: Insights from ab initio simulations. *ChemPhysChem* **7**, 1849 (2006).
- [2] Zundel, G. & Metzger, H. Energiebänder der tunnelnden Überschuss-Protonen in flüssigen Säuren. Eine IR-spektroskopische Untersuchung der Natur der Gruppierungen  $\text{H}_5\text{O}_2^+$ . *Zeit. Phys. Chem.* **58**, 225 (1968).
- [3] Wicke, E., Eigen, M. & Ackermann, T. Über den Zustand des Protons (Hydroniumions) in wäßriger Lösung. *Zeit. Phys. Chem.* **1**, 340 (1954).
- [4] Tuckerman, M., Laasonen, K., Sprik, M. & Parrinello, M. Ab initio molecular dynamics simulation of the solvation and transport of hydronium and hydroxyl ions in water. *J. Phys. Chem.* **103**, 150 (1995).
- [5] Berkelbach, T. C., Lee, H. S. & Tuckerman, M. E. Concerted Hydrogen-Bond Dynamics in the Transport Mechanism of the Hydrated Proton: A First-Principles Molecular Dynamics Study. *Phys. Rev. Lett.* **103**, 238302 (2009).
- [6] Asthagiri, D., Pratt, L. R. & Kress, J. D. Ab initio molecular dynamics and quasichemical study of  $\text{H}^+$  (aq). *Proc. Natl. Acad. Sci.* **102**, 6704 (2005).
- [7] Daly, C. A. *et al.* Decomposition of the Experimental Raman and Infrared Spectra of Acidic Water into Proton, Special Pair, and Counterion Contributions. *J. Phys. Chem. Lett.* **8**, 5246 (2017).
- [8] Dahms, F., Fingerhut, B. P., Nibbering, E. T., Pines, E. & Elsaesser, T. Large-amplitude transfer motion of hydrated excess protons mapped by ultrafast 2D IR spectroscopy. *Science* **357**, 491 (2017).
- [9] Carpenter, W. B., Fournier, J. A., Lewis, N. H. & Tokmakoff, A. Picosecond Proton Transfer Kinetics in Water Revealed with Ultrafast IR Spectroscopy. *J. Phys. Chem. B* **122**, 2792 (2018).
- [10] Calio, P. B., Li, C. & Voth, G. A. Resolving the Structural Debate for the Hydrated Excess Proton in Water. *J. Am. Chem. Soc.* **143**, 18672 (2021).
- [11] Thämer, M., De Marco, L., Ramasesha, K., Mandal, A. & Tokmakoff, A. Ultrafast 2D IR spectroscopy of the excess proton in liquid water. *Science* **350**, 78 (2015).
- [12] Fournier, J. A., Carpenter, W. B., Lewis, N. H. & Tokmakoff, A. Broadband 2D IR spectroscopy reveals dominant asymmetric  $\text{H}_5\text{O}_2^+$  proton hydration structures in acid solutions. *Nat. Chem.* **10**, 932 (2018).
- [13] Kundu, A. *et al.* Hydrated Excess Protons in Acetonitrile/Water Mixtures: Solvation Species and Ultrafast Proton Motions. *J. Phys. Chem. Lett.* **10**, 2287 (2019).
- [14] Carpenter, W. B. *et al.* Decoding the 2D IR spectrum of the aqueous proton with high-level VSCF/VCI calculations. *J. Chem. Phys.* **153**, 124506 (2020).
- [15] Marx, D., Tuckerman, M. E., Hutter, J. & Parrinello, M. The nature of the hydrated excess proton in water. *Nature* **397**, 601 (1999).
- [16] Napoli, J. A., Marsalek, O. & Markland, T. E. Decoding the spectroscopic features and time scales of aqueous proton defects. *J. Chem. Phys.* **148**, 222833 (2018).
- [17] Roy, S. *et al.* Resolving Heterogeneous Dynamics of Excess Protons in Aqueous Solution with Rate Theory. *J. Phys. Chem. B* **124**, 5665 (2020).
- [18] Komatsuzaki, T. & Ohmine, I. Energetics of proton transfer in liquid water. I. Ab initio study for origin of many-body interaction and potential energy surfaces. *Chem. Phys.* **180**, 239 (1994).
- [19] Kulig, W. & Agmon, N. A 'clusters-in-liquid' method for calculating infrared spectra identifies the proton-transfer mode in acidic aqueous solutions. *Nat. Chem.* **5**, 29 (2013).
- [20] Biswas, R., Carpenter, W., Fournier, J. A., Voth, G. A. & Tokmakoff, A. IR spectral assignments for the hydrated excess proton in liquid water. *J. Chem. Phys.* **146**, 154507 (2017).
- [21] Wang, H. & Agmon, N. Reinvestigation of the Infrared Spectrum of the Gas-Phase Protonated Water Tetramer. *J. Phys. Chem. A* **121**, 3056 (2017).



- [22] Esser, T. K. *et al.* Deconstructing Prominent Bands in the Terahertz Spectra of  $\text{H}_7\text{O}_3^+$  and  $\text{H}_9\text{O}_4^+$ : Intermolecular Modes in Eigen Clusters. *J. Phys. Chem. Lett.* **9**, 798 (2018).
- [23] Fischer, S. A. & Gunlycke, D. Analysis of Correlated Dynamics in the Grotthuss Mechanism of Proton Diffusion. *J. Phys. Chem. B* **123**, 5536 (2019).
- [24] Asmis, K. R. *et al.* Gas-Phase Infrared Spectrum of the Protonated Water Dimer. *Science* **299**, 1375 (2003).
- [25] Headrick, J. M. *et al.* Chemistry: Spectral signatures of hydrated proton vibrations in water clusters. *Science* **308**, 1765 (2005).
- [26] Guasco, T. L., Johnson, M. A. & McCoy, A. B. Unraveling anharmonic effects in the vibrational predissociation spectra of  $\text{H}_5\text{O}_2^+$  and its deuterated analogues. *J. Phys. Chem. A* **115**, 5847 (2011).
- [27] Dahms, F. *et al.* The Hydrated Excess Proton in the Zundel Cation  $\text{H}_5\text{O}_2^+$ : The Role of Ultrafast Solvent Fluctuations. *Angew. Chemie - Int. Ed.* **55**, 10600 (2016).
- [28] Tuckerman, M. E., Marx, D., Klein, M. L. & Parrinello, M. On the Quantum Nature of the Shared Proton in Hydrogen Bonds. *Science* **275**, 817 (1997).
- [29] Sauer, J. & Döbler, J. Gas-phase infrared spectrum of the protonated water dimer: Molecular dynamics simulation and accuracy of the potential energy surface. *ChemPhysChem* **6**, 1706 (2005).
- [30] Vendrell, O., Gatti, F. & Meyer, H. D. Full dimensional (15-dimensional) quantum-dynamical simulation of the protonated water dimer. II. Infrared spectrum and vibrational dynamics. *J. Chem. Phys.* **127**, 184303 (2007).
- [31] Agostini, F., Vuilleumier, R. & Ciccotti, G. Infrared spectroscopy and effective modes analysis of the protonated water dimer  $\text{H}^+(\text{H}_2\text{O})_2$  at room temperature under H/D substitution. *J. Chem. Phys.* **134**, 084303 (2011).
- [32] Marsalek, O. & Markland, T. E. Ab initio molecular dynamics with nuclear quantum effects at classical cost: Ring polymer contraction for density functional theory. *J. Chem. Phys.* **144**, 054112 (2016).
- [33] Daldrop, J. O. *et al.* Orientation of non-spherical protonated water clusters revealed by infrared absorption dichroism. *Nat. Commun.* **9**, 311 (2018).
- [34] Wolke, C. T. *et al.* Spectroscopic snapshots of the proton-transfer mechanism in water. *Science* **354**, 1131 (2016).
- [35] Wolf, S., Freier, E., Potschies, M., Hofmann, E. & Gerwert, K. Directional proton transfer in membrane proteins achieved through protonated protein-bound water molecules: A proton diode. *Angew. Chemie - Int. Ed.* **49**, 6889 (2010).
- [36] Tripathi, R., Forbert, H. & Marx, D. Settling the Long-Standing Debate on the Proton Storage Site of the Prototype Light-Driven Proton Pump Bacteriorhodopsin. *J. Phys. Chem. B* **123**, 9598 (2019).
- [37] Friedrich, D. *et al.* Collective exchange processes reveal an active site proton cage in bacteriorhodopsin. *Commun. Biol.* **3** (2020).
- [38] Yang, Y. *et al.* Ultrafast proton-coupled isomerization in the phototransformation of phytochrome. *Nat. Chem.* (2022).
- [39] Saykally, R. J. Infrared laser spectroscopy of molecular ions. *Science* **239**, 157 (1988).
- [40] Barth, A. Infrared spectroscopy of proteins. *Biochim. Biophys. Acta - Bioenerg.* **1767**, 1073 (2007).
- [41] Kramers, H. Brownian motion in a field of force and the diffusion model of chemical reactions. *Physica* **7**, 284 (1940).
- [42] Williams, G. The use of the dipole correlation function in dielectric relaxation. *Chem. Rev.* **72**, 55 (1972).
- [43] Kappler, J., Daldrop, J. O., Brüning, F. N., Boehle, M. D. & Netz, R. R. Memory-induced acceleration and slowdown of barrier crossing. *J. Chem. Phys.* **148**, 014903 (2018).
- [44] Hummer, G. From transition paths to transition states and rate coefficients. *J. Chem. Phys.* **120**, 516 (2004).
- [45] Faccioli, P., Sega, M., Pederiva, F. & Orland, H. Dominant pathways in protein folding. *Phys. Rev. Lett.* **97**, 108101 (2006).
- [46] Chung, H. S., Louis, J. M. & Eaton, W. A. Experimental determination of upper bound for transition path times in protein folding from single-molecule photon-by-photon trajectories. *Proc. Natl. Acad. Sci.* **106**, 11837 (2009).
- [47] Kim, W. K. & Netz, R. R. The mean shape of transition and first-passage paths. *J. Chem. Phys.* **143**, 224108 (2015).
- [48] Cossio, P., Hummer, G. & Szabo, A. Transition paths in single-molecule force spectroscopy. *J. Chem. Phys.* **148**, 123309 (2018).
- [49] Decka, D., Schwaab, G. & Havenith, M. A THz/FTIR fingerprint of the solvated proton: Evidence for Eigen structure and Zundel dynamics. *Phys. Chem. Chem. Phys.* **17**, 11898 (2015).
- [50] Brüning, F. N., Rammner, M., Adams, E. M., Havenith, M. & Netz, R. R. Spectral signatures of excess-proton waiting and transfer-path dynamics in aqueous hydrochloric acid solutions. *Nat. Commun.* **13**, 4210 (2022).
- [51] Schran, C. & Marx, D. Quantum nature of the hydrogen bond from ambient conditions down to ultra-low temperatures. *Phys. Chem. Chem. Phys.* **21**, 24967 (2019).
- [52] Sprik, M. & Ciccotti, G. Free energy from constrained molecular dynamics. *J. Chem. Phys.* **109**, 7737 (1998).
- [53] Daldrop, J. O., Kim, W. K. & Netz, R. R. Transition paths are hot. *Europhys. Lett.* **113**, 18004 (2016).
- [54] Cox, D. R. & Miller, H. D., *The theory of stochastic processes* (CRC Press, 1977).
- [55] Hutter, J., Iannuzzi, M., Schiffmann, F. & Vandevondele, J. CP2K: Atomistic simulations of condensed matter systems. *Wiley Interdiscip. Rev. Comput. Mol. Sci.* **4**, 15 (2014).
- [56] Kendall, R. A., Dunning, T. H. & Harrison, R. J. Electron affinities of the first-row atoms revisited. Systematic basis sets and wave functions. *J. Chem. Phys.* **96**, 6796 (1992).
- [57] Grimme, S., Antony, J., Ehrlich, S. & Krieg, H. A consistent and accurate ab initio parametrization of density functional dispersion correction (DFT-D) for the 94 elements H-Pu. *J. Chem. Phys.* **132**, 154104 (2010).
- [58] Bussi, G., Donadio, D. & Parrinello, M. Canonical sampling through velocity rescaling. *J. Chem. Phys.* **126**, 014101 (2007).
- [59] Ramírez, R., López-Ciudad, T., Kumar P, P. & Marx, D. Quantum corrections to classical time-correlation functions: Hydrogen bonding and anharmonic floppy modes. *J. Chem. Phys.* **121**, 3973 (2004).

**Supplementary information:**  
**Proton-transfer spectroscopy beyond the normal-mode scenario**

Florian N. Brünig,<sup>1</sup> Paul Hillmann,<sup>1</sup> Won Kyu Kim,<sup>2</sup> Jan O. Daldrop,<sup>1</sup> and Roland R. Netz<sup>1,\*</sup>

<sup>1</sup>*Freie Universität Berlin, Department of Physics, 14195 Berlin, Germany*

<sup>2</sup>*Korea Institute for Advanced Study, School of Computational Sciences, Seoul 02455, Republic of Korea*

(Dated: July 29, 2022)

arXiv:2109.08514v2 [physics.chem-ph] 28 Jul 2022

## I. QUANTUM ZERO-POINT MOTION EFFECTS

Quantum zero-point motion is known to smear out particle distributions and thereby to increase the particle density at barriers. Therefore in this section, we estimate the potential barrier height of a double-well potential for which the ground-state probability density develops a single minimum.

The one-dimensional stationary Schrödinger equation

$$-\frac{\hbar^2}{2m} \frac{\partial^2}{\partial d^2} \phi(d) = (U(d) - E) \phi(d) \quad (\text{S1})$$

is solved numerically for the quartic double-well potential

$$U(d) = U_0 \left( \left( \frac{d}{d_{\text{TW}}^*} \right)^2 - 1 \right)^2, \quad (\text{S2})$$

which is shown in fig. S1A to approximate the effective potential describing the excess proton distribution obtained from our ab initio molecular-dynamics (AIMD) simulations very well.

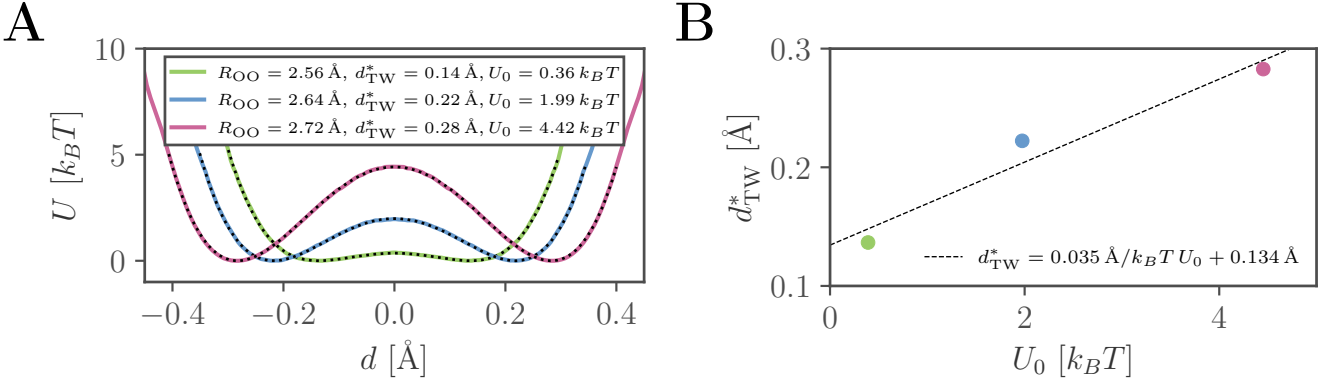


Figure S1. **A** Free-energy profiles  $U(d)$  for fixed  $R_{\text{OO}}$ , extracted from constrained ab initio molecular-dynamics (AIMD) simulations of the  $\text{H}_5\text{O}_2^+$  cation, are shown as colored lines. Fits according to eq. (S2) are shown as black dotted lines with parameters given in the legend. **B** Dependence of  $d_{\text{TW}}^*$  on  $U_0$ . Here a linear fit is shown as a black dashed line.

The equations are rescaled as

$$\frac{\partial^2}{\partial \tilde{x}^2} \phi(\tilde{x}) = (\tilde{U}(\tilde{x}) - \tilde{E}) \phi(\tilde{x}), \quad (\text{S3})$$

$$\tilde{V}(\tilde{x}) = \tilde{U}_0 (\tilde{x}^2 - 1)^2, \quad (\text{S4})$$

with  $\tilde{x} = d/d_{\text{TW}}^*$ ,  $\tilde{U}_0 = 2mU_0 d_{\text{TW}}^{*2}/\hbar^2$  and  $\tilde{E} = 2mE d_{\text{TW}}^{*2}/\hbar^2$ . Using the proton mass  $m = 1.7 \times 10^{-27}$  kg,  $\hbar = 1.1 \times 10^{-34}$  Js and  $d_{\text{TW}}^* = 0.22 \text{\AA}$  for the system with  $R_{\text{OO}} = 2.64 \text{\AA}$ , the rescaling factor for the energies is  $\hbar^2/(2md_{\text{TW}}^{*2}) = 7.4 \times 10^{-21}$  J =  $1.8 k_B T$  at 300 K. Note that this scaling factor implicitly depends on  $U_0$  due to the dependence of  $d_{\text{TW}}^*$  on  $U_0$  shown in fig. S1B.

Dimensionless ground state energies  $\tilde{E}$  are numerically computed for  $\tilde{U}_0 \in [1, 2]$  using bisection to find the eigenvalues of the dimensionless Schrödinger equation eq. (S3). The ground state energy  $\tilde{E}$  shows approximately linear dependence on  $\tilde{U}_0 \in [1, 2]$  (see green dots in fig. S2A). A minimum of the ground-state density is defined by a positive curvature at the origin,  $\frac{\partial^2}{\partial \tilde{x}^2} \phi^2(\tilde{x} = 0) > 0$ . From the Schrödinger equation eq. (S3) it becomes clear that the wave function of the ground state develops a minimum at the origin for  $\tilde{E} < \tilde{U}_0$ . It follows for the curvature of the probability density

$$\frac{\partial^2}{\partial \tilde{x}^2} \phi^2 = 2 \left[ \left( \frac{\partial \phi}{\partial \tilde{x}} \right)^2 + (\tilde{U}(\tilde{x}) - \tilde{E}) \phi^2 \right]. \quad (\text{S5})$$

\* rnetz@physik.fu-berlin.de

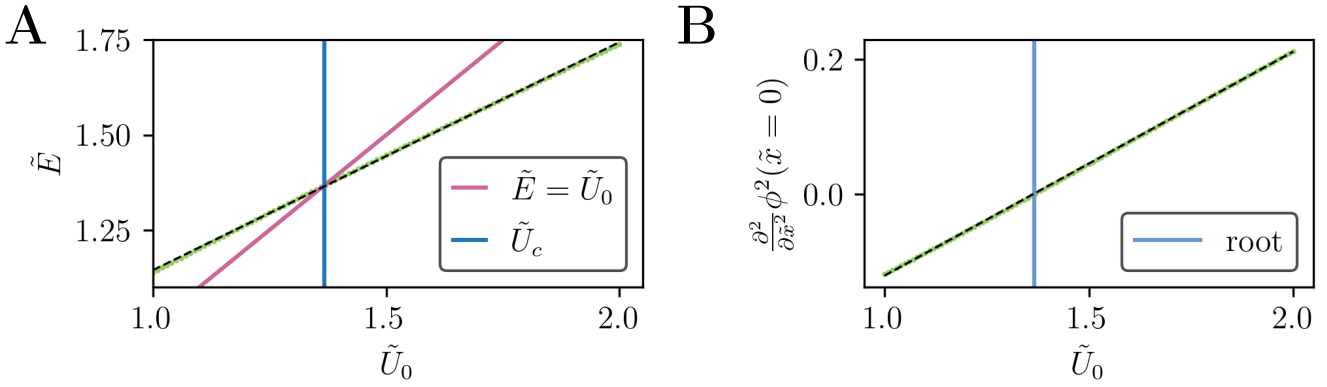


Figure S2. **A** Dimensionless ground state energy  $\tilde{E}$  as a function of the barrier height  $\tilde{U}_0$  (green dots). A linear fit according to  $\tilde{E}(U_0) = 0.601\tilde{U}_0 + 0.542$  is shown as a black dashed line. The crossing between the ground-state energy  $\tilde{E}$  and  $\tilde{E} = \tilde{U}_0$  (red line) is marked as a vertical blue line at  $\tilde{U}_c := \tilde{U}_0(\tilde{E} = \tilde{U}_0) = 1.36$ . **B** Curvature of the ground state probability density at the origin as a function of  $\tilde{U}_0$ . A linear fit according to  $\partial^2 \phi^2 / \partial \tilde{x}^2(\tilde{x} = 0) = 0.334\tilde{U}_0 - 0.455$  is shown as a black dashed line. The point where the curvature vanishes is marked as a vertical blue line, which is given by  $\tilde{U}_c = 1.36$ .

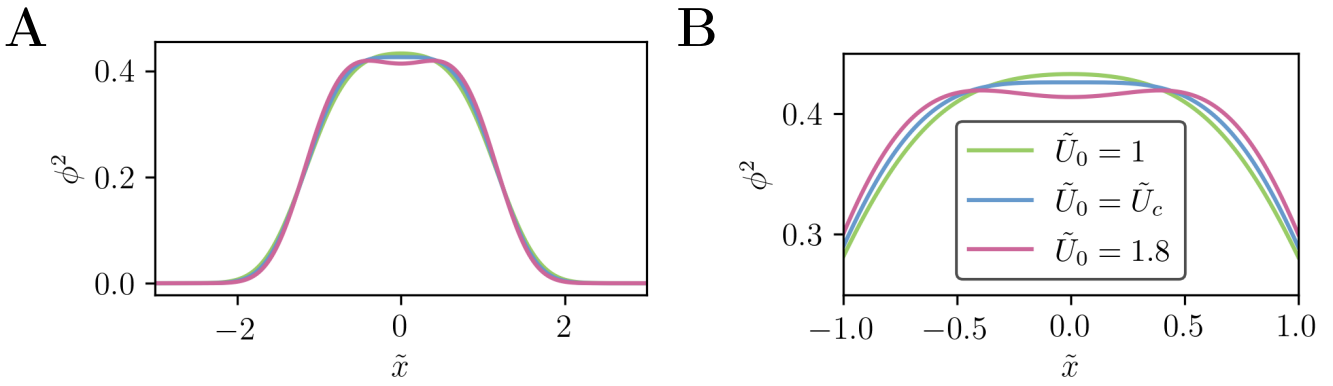


Figure S3. **A** Ground state probability densities for  $\tilde{U}_0 = 1$ ,  $\tilde{U}_0 = \tilde{U}_c$  and  $\tilde{U}_0 = 1.8$ . **B** Ground state probability densities around the origin.

Since the ground state is symmetric around the origin this becomes at the origin

$$\frac{\partial^2}{\partial \tilde{x}^2} \phi^2 = 2(\tilde{U}_0 - \tilde{E})\phi^2. \quad (\text{S6})$$

Fig. S2B shows the curvature at the origin  $\frac{\partial^2}{\partial \tilde{x}^2} \phi^2(\tilde{x} = 0)$  as a function of  $\tilde{U}_0$  (green dots). A linear fit is used to determine the critical potential strength at which the curvature vanishes as  $\tilde{U}_c = 1.36$ . Fig. S3 shows a comparison of the ground state density distributions for  $\tilde{U}_0 = \{1, \tilde{U}_c, 1.8\}$ .

From this analysis we conclude that when treating the excess proton quantum-mechanically, a minimum in the ground state probability density, reflecting the effect of the barrier, appears for barrier heights of the double-well potential

$$U_0 > \frac{\hbar^2}{2md_{\text{TW}}^*(U_0)} \tilde{U}_c k_B T, \quad (\text{S7})$$

which holds for  $U_0 > 2.5 k_B T$  as can be read off fig. S4. Therefore, using the naive assumption that a minimum in the probability density at the barrier top indicates the presence of an effective quantum-mechanical barrier, which is far from obvious, one could speculate that the presented results for the spectroscopic signatures of proton barrier-crossing are expected to survive quantum-mechanical zero-point motion effects for high enough potential barriers.

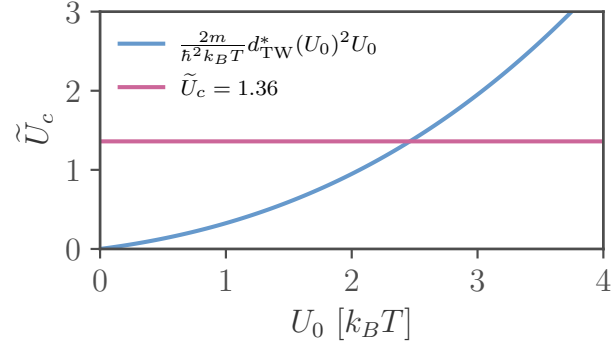


Figure S4. A minimum in the ground state probability density appears for  $\frac{2m}{\hbar^2 k_B T} d_{\text{TW}}^*(U_0)^2 U_0 > \tilde{U}_c$  as a rearrangement of eq. (S7) with  $U_0$  being the barrier height of the double-well potential,  $\tilde{U}_c = 1.36$  taken from fig. S2B and  $d_{\text{TW}}^*(U_0)$  taken from the linear fit in fig. S1B.

## II. SUMMARY OF PREVIOUS EXPERIMENTAL AND THEORETICAL STUDIES ON INFRARED SPECTRA OF THE $\text{H}_5\text{O}_2^+$ CATION

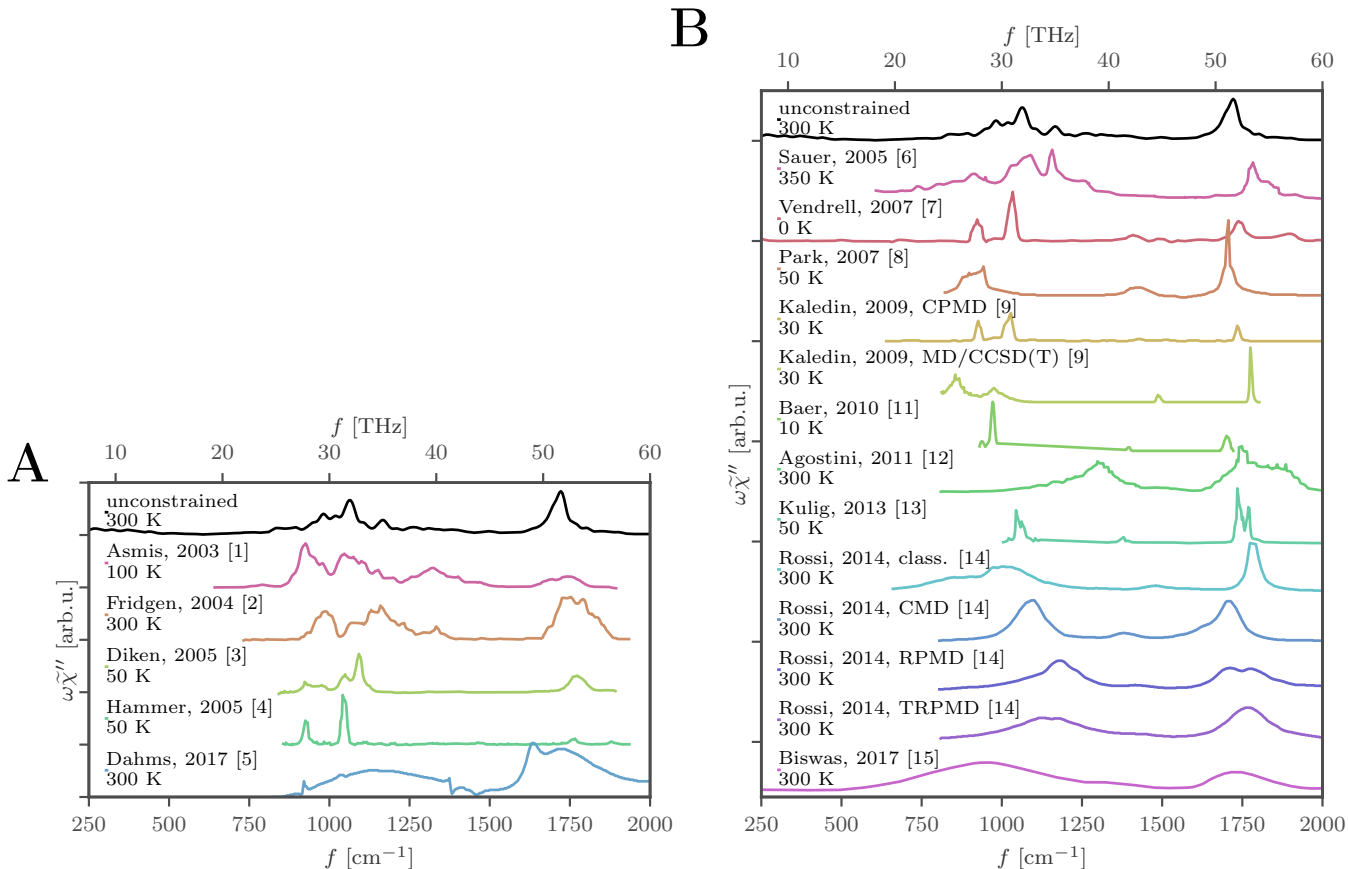


Figure S5. Collection of experimental (A) and theoretical (B) IR spectra of the  $\text{H}_5\text{O}_2^+$  cation in the proton-transfer regime (colored lines), compared to the IR spectrum obtained from AIMD simulations in this study, shown in black. **A** The experimental spectra were recorded using multiple-photon-dissociation (IRPMD) spectroscopy [1, 2], predissociation (IRPD) spectroscopy in Argon [3] and Neon [4] and Fourier-transform IR (FTIR) spectroscopy of  $\text{H}_5\text{O}_2^+$  cations solvated in acetonitrile [5]. **B** Theoretical spectra were obtained using AIMD simulations on the MP2/cc-pVTZ level [6], the multiconfiguration time-dependent Hartree (MCTDH) method [7], CPMD simulations using the BLYP functional [8], CPMD simulations using the BLYP functional [9], MD simulations on the CCSD(T) potential energy surface using MP2 dipole moment functions (based on [10]) [9], AIMD simulations on the BLYP-D3 TZV2P level [11], MD simulations using the multistate-empirical-valence-bond (MS-EVB) method [12], AIMD simulations on the DZVP-BLYP level [13], classical MD, centroid MD (CMD), as well as ring polymer MD simulations (RPMD, TRPMD)[14] on the CCSD(T) potential energy surface [10] and normal mode analysis on the 6-311++G(d,p)-B3LYP level performed on states obtained from a multistate-empirical-valence-bond (MS-EVB) MD simulation [15]. All theoretical results were obtained for a single  $\text{H}_5\text{O}_2^+$  cation, except for [15], who computed the spectra from clusters of 16–18 water molecules and an excess-proton.

A collection of IR spectra of the  $\text{H}_5\text{O}_2^+$  cation in the so-called proton-transfer regime,  $600\text{ cm}^{-1}$  to  $1500\text{ cm}^{-1}$ , obtained from experiments is given in fig. S5A and from theoretical calculations in fig. S5B. The spectra are compared to the spectrum of the unconstrained  $\text{H}_5\text{O}_2^+$  cation obtained from AIMD simulations in this study (black lines on top). The spectra vary greatly among different experimental studies in this regime, highlighting the subtle differences between experimental techniques and also pointing to a pronounced temperature dependence of the spectra. Fridgen et al. [2] say that “at this point, we are unable to determine the source of the discrepancy between the present infrared spectrum and that obtained by Asmis et al. [1]”. Sauer and Döbler [6] discuss “that differences between the IRPMD spectrum [1] and the IRPD spectrum [3] should be due to the different excitation mechanisms and/or different temperatures”. Hammer et al. [4] state “the IR profiles obtained in these two measurements [1, 2] were markedly different, perhaps reflecting the different ion sources used in the two experiments and/or the specific fluence characteristics of the laser sources”. Vendrell et al. [7] introduce the topic stating that “spectra could not be consistently assigned in terms of

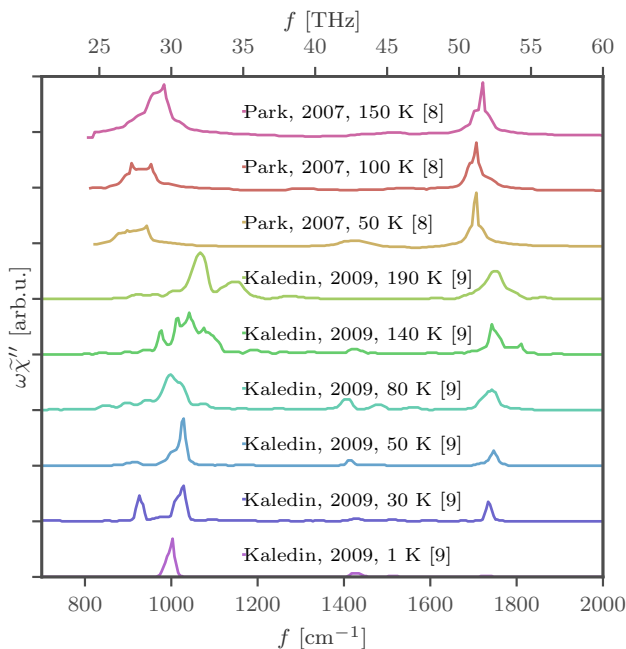


Figure S6. Comparison of theoretical IR spectra of the  $\text{H}_5\text{O}_2^+$  cation in the proton-transfer regime at various temperatures obtained from Car-Parinello MD (CPMD) simulations using the BLYP density functional method [8, 9].

fundamental frequencies and overtones of harmonic vibrational modes due to large amplitude anharmonic displacements and couplings of the cluster [1, 2, 4, 16]” and conclude their study by pointing out that their “reported calculations are in excellent agreement to the experimental measurements of Refs. [4, 16] on the predissociation spectrum of  $\text{H}_5\text{O}_2^+\cdot\text{Ne}$ ”, which is the most widely accepted low-temperature spectrum to date. Furthermore, nuclear quantum effects were studied in detail by Rossi et al. [14], who compared spectra from different ring polymer MD simulations, and Park et al. [8] and Baer et al. [11] successfully investigated the messenger-induced changes of spectra apparent in IRMPD techniques. The temperature dependence was analyzed by Park et al. [8] and Kaledin et al. [9] in Car-Parinello MD (CPMD) simulations, presented in fig. S6, and classical MD simulations on the CCSD(T) potential energy surface using MP2 dipole moment functions (based on [10]), stating that “classical MD simulations at a temperature of 30 K qualitatively reproduce many of the key features in the experimental vibrational [Ar-] predissociation”. More recent studies have focused on the  $\text{H}_5\text{O}_2^+$  cation in larger water clusters or in bulk water or other solvents and at room temperature [5, 12, 13, 15, 17, 18]. These studies identify remarkably broad IR features in the  $1000\text{ cm}^{-1}$  to  $1200\text{ cm}^{-1}$  regime, associated with “proton shuttling” [17], the “proton-transfer mode (PTM)” [5, 13, 15] or the “shared proton stretch” [18].

The review of the published experimental and theoretical data shows that the data produced in this study is in qualitative agreement with previous results. However, especially in the region of  $800\text{ cm}^{-1}$  to  $1200\text{ cm}^{-1}$  associated with the proton-transfer motion, large temperature and system-dependent differences between the previously published results are observed and reflect the incomplete understanding of proton-transfer dynamics.

### III. NORMAL-MODE ANALYSIS OF THE $\text{H}_5\text{O}_2^+$ CATION

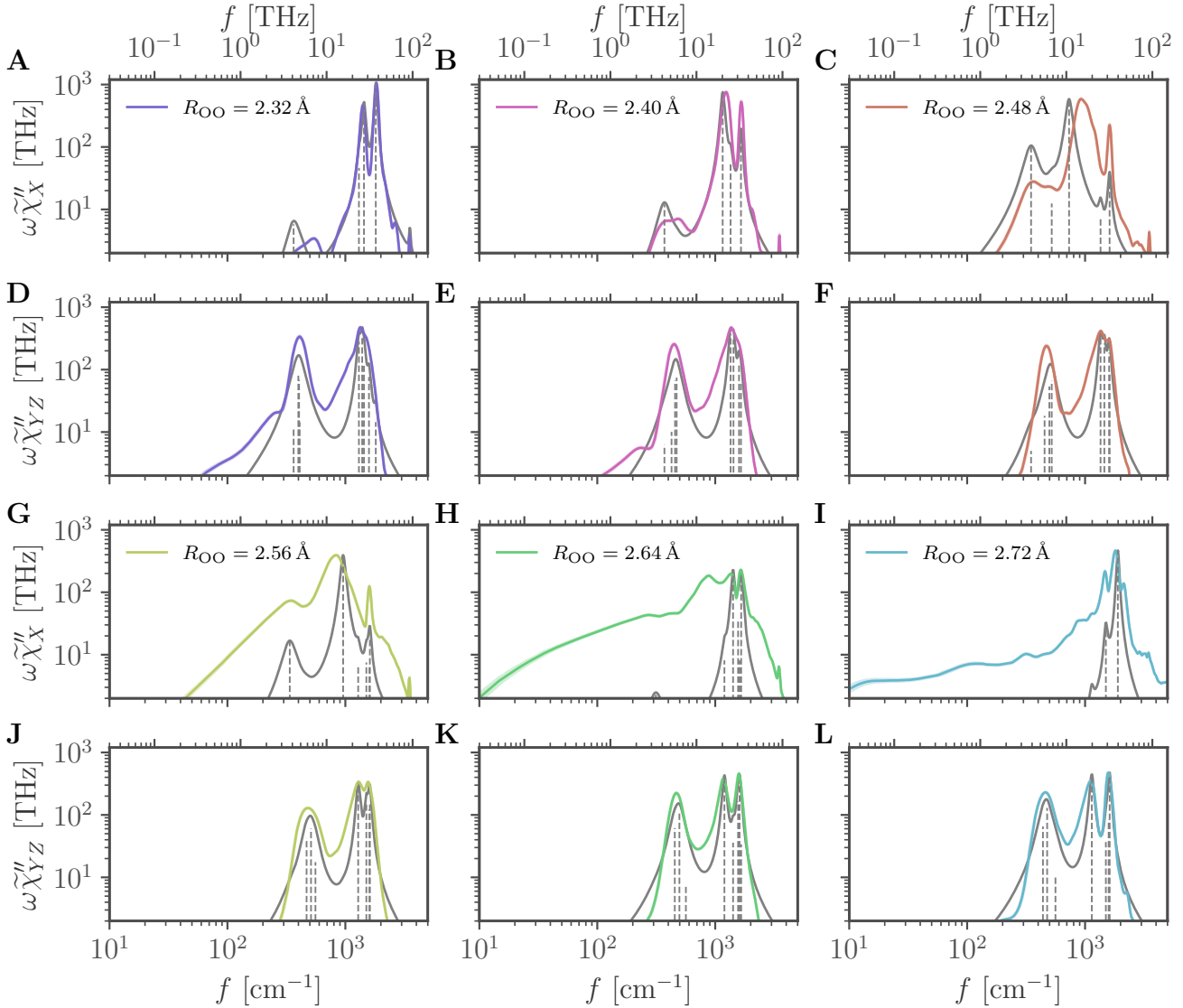


Figure S7. IR spectra of the excess proton (colored lines) in the  $\text{H}_5\text{O}_2^+$  cation for different constraint oxygen distances  $R_{\text{OO}}$  compared to normal-mode spectra calculated from energetically optimized structures and projected on the proton coordinate (grey dashed sticks). The discrete normal modes sum to smooth spectra (grey lines) by including line-broadening at finite temperature obtained from damped harmonic oscillations of the normal modes according to eq. S36 in section X and assuming a friction coefficient of  $\gamma = 16$  u/ps. The spectra are shown for different orientations (**A–C**, **G–I**:  $x$ -axis connecting the two oxygens, **D–F**, **J–L**:  $yz$ -plane).

The normal modes are obtained as the Eigenvectors of the Hessian of the optimal structure in a chosen coordinate system, the Eigenvalues give the frequencies. The normal-mode analysis of the  $\text{H}_5\text{O}_2^+$  systems was performed for energetically optimized structures using the same set of parameters as for the AIMD simulation.

A projection of the Eigenvectors on the proton coordinate allows to obtain the relative magnitudes of the excess-proton spectra predicted from the normal-mode analysis. These are scaled to the magnitudes of the excess-proton spectra obtained directly from the AIMD simulations for various  $R_{\text{OO}}$  and orientations in fig. S7. To improve the normal-mode spectra, line-broadening of the normal modes at finite temperature is modeled by damped harmonic oscillations (see SI section X). In the  $yz$ -plane the agreement is very good for all barrier heights indicating, that the method is well suited for modeling the excess-proton dynamics without a barrier. Along  $x$  the normal mode spectra serve to explain the



major peaks of the spectra at high frequencies which will be identified as the normal-mode contributions. The broad low-frequency shoulder, which is related to the barrier-crossing effects, can obviously not be modeled using normal modes.

The system with  $R_{\text{OO}} = 2.40 \text{ \AA}$  represents the global unconstrained minimum of the free-energy landscape, shown in fig. 1D in the main text, and can therefore be used to compare qualitatively to published data on the unconstrained  $\text{H}_5\text{O}_2^+$  cation, as done in tab. S1 for the range  $100 \text{ cm}^{-1}$  to  $2000 \text{ cm}^{-1}$ . The normal-modes can be grouped to rocking and wagging modes in the range  $300 \text{ cm}^{-1}$  to  $600 \text{ cm}^{-1}$ , the water-water stretch at around  $550 \text{ cm}^{-1}$  to  $650 \text{ cm}^{-1}$ , which is missing in the constrained case, the widely discussed proton-transfer mode along  $x$ , which varies greatly between  $800 \text{ cm}^{-1}$  to  $1200 \text{ cm}^{-1}$ , a pair of modes between  $1300 \text{ cm}^{-1}$  to  $1600 \text{ cm}^{-1}$ , associated with perpendicular excess-proton motion in the  $yz$ -plane, and the two water-bending modes at  $1600 \text{ cm}^{-1}$  to  $1800 \text{ cm}^{-1}$ , for which the lower one shows excess-proton motion in the  $yz$ -plane (named in-phase or gerade) and the higher one shows excess-proton motion along  $x$  (named out-of-phase or ungerade).

Illustrations of the normal modes in the range  $100 \text{ cm}^{-1}$  to  $2000 \text{ cm}^{-1}$  of  $\text{H}_5\text{O}_2^+$  cations with various constrained  $R_{\text{OO}}$  are shown in fig. S8, where the colored frames indicate similar normal modes for different values of  $R_{\text{OO}}$ . Fig. S9 summarizes the frequencies of the normal modes for all values of  $R_{\text{OO}}$  and highlights the associated relative excess-proton-motion intensities either along  $x$  or in the  $yz$ -plane. Most modes shift only weakly, including the wagging and rocking modes in the range  $300 \text{ cm}^{-1}$  to  $600 \text{ cm}^{-1}$  and the pair of modes between  $1300 \text{ cm}^{-1}$  to  $1600 \text{ cm}^{-1}$ , associated with perpendicular excess-proton motion in the  $yz$ -plane. However, the proton-transfer mode ( $1157 \text{ cm}^{-1}$  for  $R_{\text{OO}} = 2.40 \text{ \AA}$ ) strongly increases for values of  $R_{\text{OO}} \geq 2.40 \text{ \AA}$ , as shown previously by Wolke et al. [19] for the  $\text{D}_5\text{O}_2^+$  cation, which possibly explains why the proton-transfer mode in bulk is suggested to reside at much higher wavenumbers compared to the gas-phase spectra [13]. The in-phase water bending mode shows no shifting but the out-of-phase water bending mode, associated with excess-proton motion along  $x$ , strongly shifts. Generally, modes associated with proton motion along  $x$  are shown to be highly sensitive on the value of  $R_{\text{OO}}$ , while modes that are associated with proton motion in the  $yz$ -plane are not.

Table S1. Collection of previous identifications of normal modes in the  $\text{H}_5\text{O}_2^+$  cation in the range  $100\text{ cm}^{-1}$  to  $2000\text{ cm}^{-1}$ , compared to data obtained in this study with constrained  $R_{\text{OO}} = 2.40\text{ \AA}$  in the first row. Bold fonts indicate significant motion of the excess proton (if reported).

BLYP-D3, TZV2P, $R_{\text{OO}} = 2.40\text{ \AA}$	wagging, rocking	320, 426, <b>456</b> , <b>470</b>	p. trans. ( $x$ )	<b>1157</b>	proton perp. ( $yz$ )	<b>1350</b> , <b>1428</b>	water bend	<b>1591</b> , <b>1653</b>
MP2, aug-cc-pVTZ [6]	$\text{H}_2\text{O}$ wag, $\text{H}_2\text{O}$ rock	362, 461, 532, 535	sym. OHO str.	627	OHO bend ( $y, z$ )	1484, 1557	HOH bend	1710, 1765
MP2, cc-pVTZ [6]		367, 451, 522, 529	asym. OHO str.	631		1493, 1572	(in/out phase)	1710, 1773
MP2, cc-pVTZ(aug-O) [6]		347, 456, 525, 532,		626		1473, 1551		1706, 1761
CCSD(T), cc-pVTZ [6]		350, 457, 531, 535		633		1493, 1572		1724, 1780
CCSD(T), MP2, aug-cc-pVTZ [10]		339, 471, 532, 554		630		1494, 1574		1720, 1770
MP2, aug-cc-pVTZ [4]			OHO stretch	808			HOH bend	1662, 1717
MCTDH [7]	wagging	106, 108, 232, 254, 374, 422	p. trans. doub.	<b>918</b> , <b>1033</b>	proton perp. p. trans. + wat. str.	<b>1391</b>	water bend	<b>1606</b> , <b>1741</b>
	rocking	481, 915, 930, 943				<b>1411</b>	(gerade, unger.)	
BLYP, aug-cc-pVTZ [8]			asym. OHO str.	938	OHO bend ( $y, z$ )	1408, 1478	HOH bend	1647, 1702
B3LYP, aug-cc-pVTZ [8]				891		1397, 1455		1619, 1678
MP2, aug-cc-pVTZ [8]				868		1405, 1478		1627, 1680
BLYP-D3, TZV2P, AIMD [11]	wagging, rocking	370, 431, 498, 514	OO stretch	571	proton $_{yz}$ ( $\gamma_p, \gamma'_p$ )	<b>1396</b> , <b>1477</b>	water bend ( $\delta_s, \delta_a$ )	<b>1636</b> , <b>1700</b>
MS-EVB, EMA [12]				1032		1311, 1560		1638, 1769
B3LYP, aug-cc-pVTZ [13]				926		1446		1742

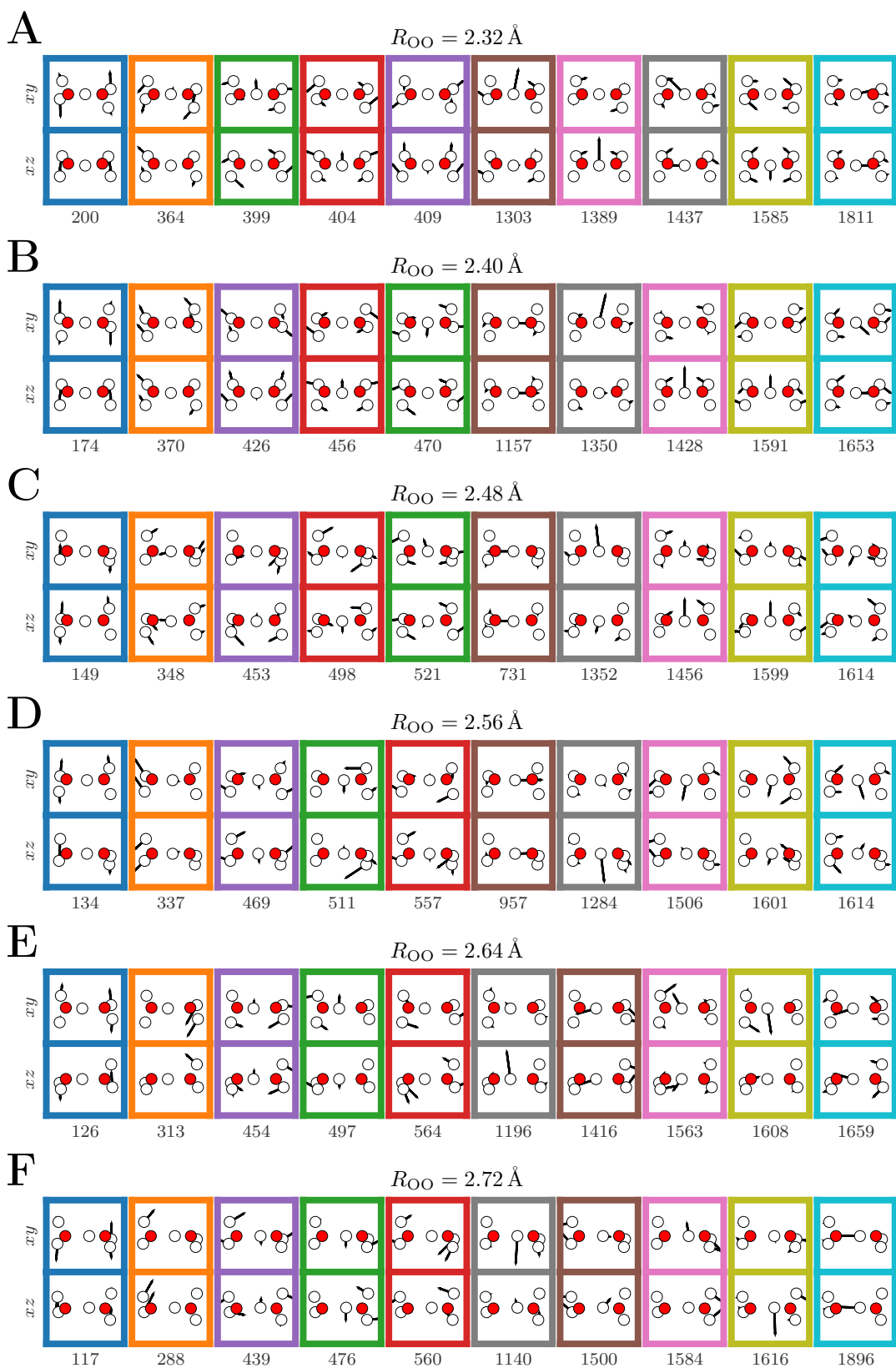


Figure S8. Illustrations of the normal modes of the  $\text{H}_5\text{O}_2^+$  cation for various constrained  $R_{OO}$ , projected on the  $xy$  and  $xz$  planes. The colored frames guide the eye through the shifting of a respective normal mode through A-F.

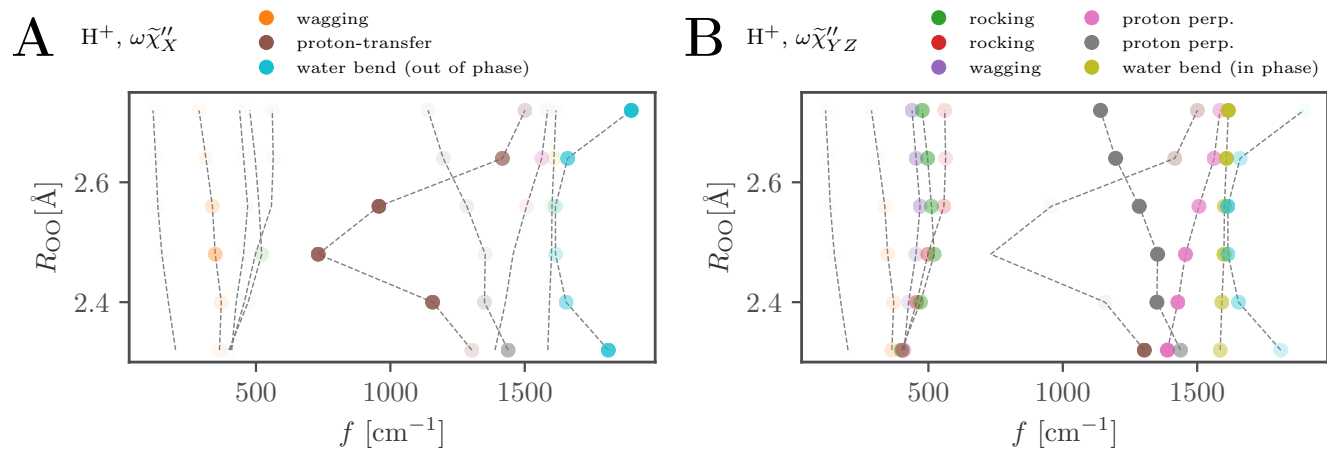


Figure S9. Normal mode frequencies of the excess-proton dynamics in the  $\text{H}_5\text{O}_2^+$  cation for various constrained  $R_{\text{OO}}$  as shown in fig. S7. The shading indicates the relative amplitudes of the respective normal modes, normalized to the maximal amplitude for each value of  $R_{\text{OO}}$ . The colors and grey dashed lines guide the eye through the shifting of a respective normal mode, as also shown in fig. S8.

#### IV. DECOMPOSITION OF THE $\text{H}_5\text{O}_2^+$ IR SPECTRA INTO EXCESS-PROTON AND WATER CONTRIBUTIONS

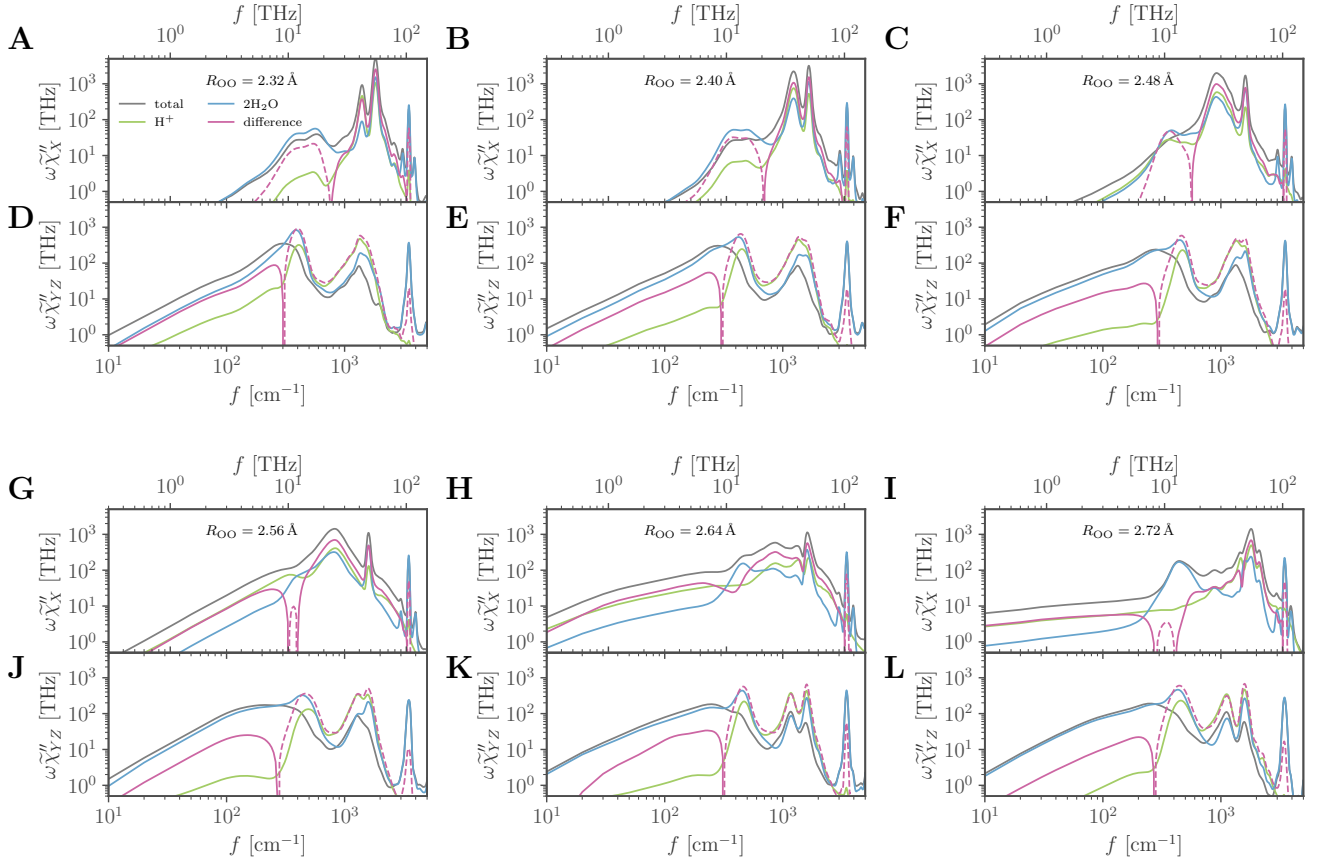


Figure S10. Decomposition of the IR spectra of the  $\text{H}_5\text{O}_2^+$  cation with two constrained oxygens at a given distance  $R_{\text{OO}}$  in different directions (**A–C**, **G–I**: along the  $x$ -axis connecting the two oxygens, **D–F**, **J–L**: along the  $yz$ -plane) into water and excess-proton contributions. The total IR spectra are shown in grey, the spectra of the excess proton in green and the spectra of the two water molecules in blue. The cross-correlation spectrum defined as  $\tilde{\chi}_{\text{H}^+, \text{H}_2\text{O}}'' = \tilde{\chi}_{\text{tot}}'' - \tilde{\chi}_{\text{H}^+}'' - \tilde{\chi}_{\text{H}_2\text{O}}''$  is shown in red. The dashed red line denotes negative values of the cross-correlation spectrum.

By using Wannier centers for charge localization, the total dipole moment of the simulation systems can be exactly decomposed into proton and water contributions  $\mathbf{p}_{\text{tot}}(t) = \mathbf{p}_{\text{H}^+}(t) + \mathbf{p}_{\text{H}_2\text{O}}(t)$ . A comparison of the IR spectra of the total dipole moment  $\omega\tilde{\chi}_{\text{tot}}''$  of the  $\text{H}_5\text{O}_2^+$  cation for various constrained oxygen positions to the power spectra of only the excess proton  $\omega\tilde{\chi}_{\text{H}^+}''$  and the power spectra of the dipole moments of the two flanking water molecules  $\omega\tilde{\chi}_{\text{H}_2\text{O}}''$  is shown in fig. S10A–L in different directions. As discussed in SI section VII, the cross-correlation spectra  $\omega\tilde{\chi}_{\text{H}^+, \text{H}_2\text{O}}''$ , shown in red in fig. S10A–L, are proportional to the cross-correlations of water-dipole-moment and excess-proton dynamics. Along  $x$ , the cross-correlation spectra of the six systems shown here, are nearly entirely positive as well as nearly proportional to the power spectrum of the proton itself, indicating constructive coupling of the proton motion to the water dipole moments along this axis, as previously shown [6]. An apparent exception to this is the rocking and wagging regime at  $300\text{ cm}^{-1}$  to  $600\text{ cm}^{-1}$  and the split OH-stretching mode at around  $3500\text{ cm}^{-1}$ , which shows a strong negative cross-correlation spectrum in both  $x$  direction and  $yz$ -plane. Adjacent to this band all systems show two weak OH-stretching vibrations along  $x$ , likely a Stark effect of the mean excess-proton field on the water dipole moments.

In the  $yz$ -plane the cross-correlation spectra are nearly entirely negative, indicating mainly out-of-phase motion of the excess-proton and the water dipole moments, producing generally weaker spectra in  $yz$  compared to  $x$ .

It can be concluded that the IR spectrum of the  $\text{H}_5\text{O}_2^+$  cation along the axis connecting the two water oxygens reflects the excess-proton dynamics. This justifies the IR signal to be used as a reporter of the excess-proton dynamics, as well as the focus on its dynamics.

## V. COMPARISON OF CONSTRAINED AND UNCONSTRAINED DICHOIC IR SPECTRA OF THE $\text{H}_5\text{O}_2^+$ CATION

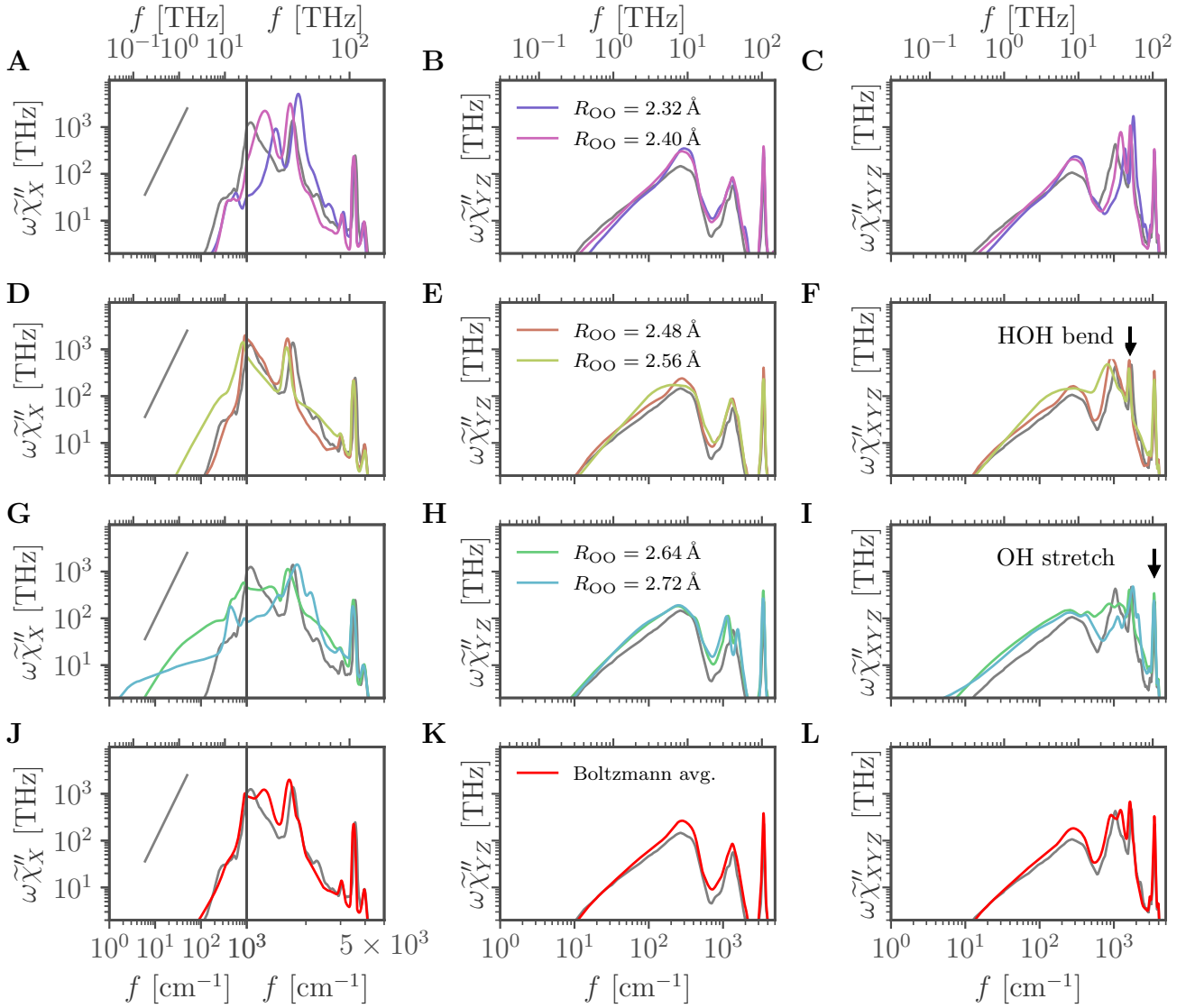


Figure S11. IR spectra of the  $\text{H}_5\text{O}_2^+$  cation in different directions (**A**, **D**, **G**, **J**: along the  $x$ -axis connecting the two oxygens, **B**, **E**, **H**, **K**: along the  $yz$ -plane **C**, **F**, **I**, **L**: isotropic spectrum). **A–I** The colors correspond to systems with different fixed oxygen-oxygen separation  $R_{\text{OO}}$ , grey lines denote the unconstrained system. **J–L** Comparison of the IR spectra of the unconstrained system (grey lines) to a Boltzmann average (red lines) according to eq. (S8) of the spectra in **A–I**. The HOH-bending mode and OH-stretching mode of the water molecules are indicated in **F** and **I**. The short straight grey lines indicate the  $\omega^2$ -scaling associated with the low-frequency shoulder of the power spectra.

IR spectra of the unconstrained  $\text{H}_5\text{O}_2^+$  cation and various systems with constrained  $R_{\text{OO}}$  are shown in fig. S11 in different directions. The  $x$ -axis corresponds to the direction connecting the two oxygens, while the  $yz$ -plane is orthogonal to that axis, as illustrated in fig. 1A in the main text. Interestingly, the spectra in  $x$ -direction strongly depend on the value of the constrained oxygen separation  $R_{\text{OO}}$  for frequencies lower than  $2500 \text{ cm}^{-1}$  (figs. S11A, S11D, S11G and S11J). The HOH-bending mode is shifted to almost  $2000 \text{ cm}^{-1}$  for  $R_{\text{OO}} = 2.32 \text{ \AA}$  (fig. S11A) and to slightly lower frequencies than the unconstrained system for  $R_{\text{OO}} \geq 2.40 \text{ \AA}$  (figs. S11D and S11G), whereas the frequency of the OH-stretching mode is not affected by fixing  $R_{\text{OO}}$ .

The various spectra for the  $yz$ -plane in figs. S11B, S11E, S11H and S11K are indistinguishable on the other hand.

The dominant features are the librations of the water molecules at  $300\text{ cm}^{-1}$  and the OH-stretching mode at around  $3500\text{ cm}^{-1}$ . While the OH-stretching mode appears in both directions, the HOH-bending mode is mainly visible along the  $x$ -axis. Note that in the  $yz$ -plane the HOH-bending mode contributions of the outer hydrogens of each water molecule cancel out due to symmetric motion with respect to the  $x$ -axis.

The isotropic spectra in figs. S11C, S11F, S11I and S11L depend on  $R_{OO}$  only in the regime  $400\text{ cm}^{-1}$  to  $1700\text{ cm}^{-1}$  since for lower frequencies, between  $10\text{ cm}^{-1}$  to  $400\text{ cm}^{-1}$ , the  $yz$ -contributions to the isotropic spectrum are dominant. In particular, this motivates the analysis of dynamics along  $x$ -direction, which shows the dominant contribution to the isotropic spectrum except for very low frequencies.

Interestingly, the spectra of the unconstrained systems are well recovered by a Boltzmann average of the spectra of the systems with fixed  $R_{OO}$  according to

$$\omega\tilde{\chi}''(\omega)_{\langle R_{OO} \rangle} = \frac{\sum_i \omega\tilde{\chi}''(\omega)_{R_{OO_i}} e^{-U(R_{OO_i})/k_B T}}{\sum_i e^{-U(R_{OO_i})/k_B T}}, \quad (\text{S8})$$

using the free energy along  $R_{OO}$  of the unconstrained system,  $U(R_{OO})$ , shown in fig. 1D in the main text. As shown in figs. S11J, fig. S11K and fig. S11L, the agreement is very good along all directions, which indicates a sufficient dynamic decoupling of the slow oxygen coordinate  $R_{OO}$  from the proton coordinate  $d$  with respect to IR spectra and allows observations for the constrained systems to be generalized to the unconstrained system.

## VI. RECROSSING TRANSFER PATHS OF THE EXCESS-PROTON IN THE $\text{H}_5\text{O}_2^+$ CATION

After crossing the barrier once, the excess proton often immediately recrosses the barrier. In order to quantify this effect, the transfer paths are grouped into transfer events. A transfer event is defined by subsequently occurring transfer paths without recrossing of the same minimum and is sorted by the number of these crossings. An example for this definition is given in fig. S12A. The normalized distribution of the transfer events by the number of recrossings, in the following called the recrossing-number distribution  $p_{\text{RN}}(n)$ , is given in fig. S12B. For low barriers up to 40 subsequent recrossings are observed. For higher barriers the distribution is shifted to lower numbers of recrossings. Nevertheless, for all barrier heights a significant fraction of transfer events consist of multiple recrossings,  $\sum_{i=1}^{\infty} p_{\text{RN}}(n) = 0.47$  for  $R_{OO} = 2.56\text{ \AA}$ ,  $0.32$  for  $R_{OO} = 2.64\text{ \AA}$  and  $0.14$  for  $R_{OO} = 2.72\text{ \AA}$ . The mean number of recrossings is  $\sum_{i=0}^{\infty} n p_{\text{RN}}(n) = 1.84$  for  $R_{OO} = 2.56\text{ \AA}$ ,  $0.70$  for  $R_{OO} = 2.64\text{ \AA}$  and  $0.41$  for  $R_{OO} = 2.72\text{ \AA}$ .

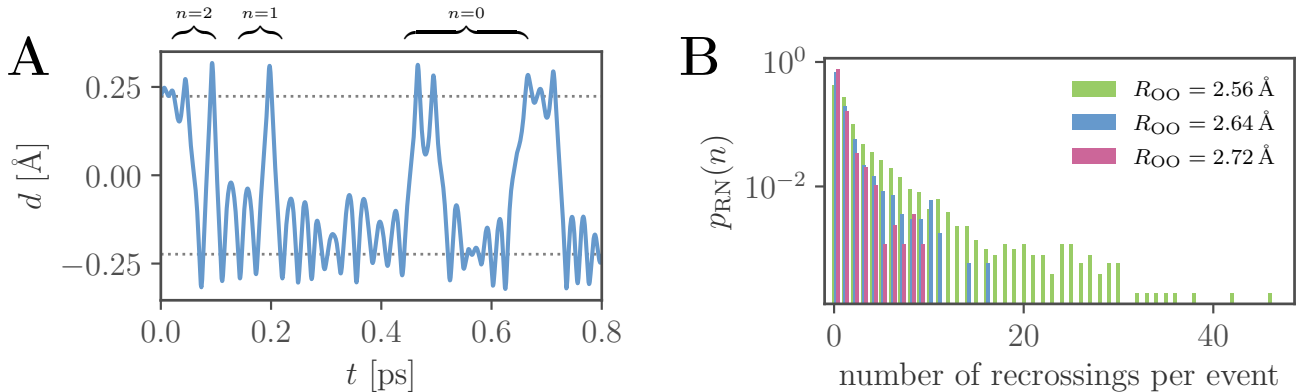


Figure S12. **A** Example trajectory of the excess-proton coordinate  $d(t)$  in the  $\text{H}_5\text{O}_2^+$  cation with constrained  $R_{OO}=2.64\text{ \AA}$ , showing nine transfer paths between the minima of the free energy denoted as grey dotted lines. The first three transfer paths belong to a single transfer event (with two recrossings). The subsequent two transfer paths also belong to a single transfer event (with one recrossing). The remaining four transfer paths are all defined not to be recrossing. It follows  $p_{\text{RN}}(0) = 4/6$ ,  $p_{\text{RN}}(1) = 1/6$  and  $p_{\text{RN}}(2) = 1/6$ . **B** Recrossing-number probability distributions  $p_{\text{RN}}(n)$  normalized such that  $\sum_{n=0}^{\infty} p_{\text{RN}}(n) = 1$ , for different  $R_{OO}$ .

## VII. IR POWER SPECTRA FROM LINEAR-RESPONSE THEORY

Assuming linear response of an observable  $x(t)$  with respect to a force that couples to an observable  $y(t)$ , the response function  $\chi_{xy}(t)$  is related to the correlation function  $C_{xy}(t') = \langle x(t+t')y(t) \rangle$

$$\chi_{xy}(t) = -\frac{1}{k_B T} \Theta(t) \frac{d}{dt} C_{xy}(t), \quad (\text{S9})$$

where  $k_B T$  is the thermal energy. Realizing that  $\chi(t)$  is single-sided, the Fourier transform is calculated as

$$\begin{aligned} \tilde{\chi}_{xy}(\omega) &= -\frac{1}{k_B T} \int_0^\infty dt e^{i\omega t} \frac{d}{dt} C_{xy}(t) \\ &= -\frac{1}{k_B T} \left( C_{xy}(0) - i\omega \int_0^\infty dt e^{i\omega t} C_{xy}(t) \right) \\ &= -\frac{1}{k_B T} \left( C_{xy}(0) - i\omega \tilde{C}_{xy}^+(\omega) \right), \end{aligned} \quad (\text{S10})$$

where the superscript  $+$  denotes a single-sided Fourier transform. In case of  $x = y$ ,  $C_{xx}(t)$  is an autocorrelation function, which is real and symmetric, therefore it follows for the imaginary part of the response function in Fourier space

$$\tilde{\chi}_{xx}''(\omega) = \frac{1}{k_B T} \omega \text{Re}(\tilde{C}_{xx}^+(\omega)) \quad (\text{S11})$$

$$= \frac{1}{k_B T} \frac{\omega}{2} \tilde{C}_{xx}(\omega). \quad (\text{S12})$$

When computing the power spectra of a stochastic process  $x(t)$ , limited to the time domain  $[0, L_t]$ , the Wiener-Kintchine theoreme, eq. (S64) in section XVI, can be used to express  $\tilde{C}_{xx}(\omega)$  in terms of  $\tilde{x}(\omega)$ , turning eq. (S12) into

$$\tilde{\chi}_{xx}''(\omega) = \frac{\omega}{2k_B T L_t} |\tilde{x}(\omega)|^2. \quad (\text{S13})$$

In case of  $x(t)$  being the polarization  $\mathbf{p}(t)$  of the system, which is coupled to an external electric field  $\mathbf{E}(t)$ , the dimensionless dielectric susceptibility  $\chi(t)$  is given by

$$\tilde{\chi}(\omega) = \frac{1}{V \epsilon_0 l} \langle \tilde{\chi}_{\mathbf{p}\mathbf{p}}(\omega) \rangle, \quad (\text{S14})$$

where  $\epsilon_0$  is the vacuum permittivity,  $V$  is the system volume and an average is performed over the  $l$  dimensions of  $\mathbf{p}$ .

## VIII. SPECTRAL CROSS CONTRIBUTIONS OF EXCESS-PROTON DYNAMICS IN THE $\text{H}_5\text{O}_2^+$ CATION

A decomposition of a trajectory  $x(t)$  into two parts  $x(t) = x_1(t) + x_2(t)$  gives rise to three contributions in the total power spectrum

$$\begin{aligned} \omega \tilde{\chi}_{xx}''(\omega) &= \frac{\omega^2}{2k_B T} \left[ \tilde{C}_1(\omega) + \tilde{C}_2(\omega) + 2\tilde{C}_{1,2}(\omega) \right] \\ &= \omega \left[ \tilde{\chi}_1''(\omega) + \tilde{\chi}_2''(\omega) + \tilde{\chi}_{1,2}''(\omega) \right], \end{aligned} \quad (\text{S15})$$

where the cross-correlation contribution  $\tilde{\chi}_{1,2}''(\omega)$  is defined such that it equals the difference spectrum

$$\begin{aligned} \tilde{\chi}_{\text{diff}}''(\omega) &= \tilde{\chi}_{xx}'' - \tilde{\chi}_1''(\omega) - \tilde{\chi}_2''(\omega) = \tilde{\chi}_{1,2}''(\omega) \\ &= \frac{\omega}{k_B T} \tilde{C}_{1,2}(\omega). \end{aligned} \quad (\text{S16})$$

A positive cross-correlation spectrum hints to in-phase motion, a negative cross-correlation spectrum to out-of-phase motion of  $x_1(t+t')$  and  $x_2(t)$  at a given frequency.

Therefore the decomposition of the excess-proton dynamics in the time domain according to  $d(t) = d_{\text{TW}}(t) + d_{\text{TP}}(t) + d_{\text{NM}}(t)$  into a transfer-waiting  $d_{\text{TW}}(t)$ , a transfer-path  $d_{\text{TP}}(t)$  and a normal-mode contribution  $d_{\text{NM}}(t)$  as introduced in fig. 2, in the main text, produces spectral cross-contributions. The spectral contributions  $\omega \tilde{\chi}_{\text{TW}}''$ ,  $\omega \tilde{\chi}_{\text{TP}}''$  and  $\omega \tilde{\chi}_{\text{NM}}''$  as well as the spectral cross contributions  $\omega \tilde{\chi}_{\text{TW,NM}}''$ ,  $\omega \tilde{\chi}_{\text{TP,TW}}''$  and  $\omega \tilde{\chi}_{\text{NM,TP}}''$  resulting from this decomposition are shown in fig. S13.



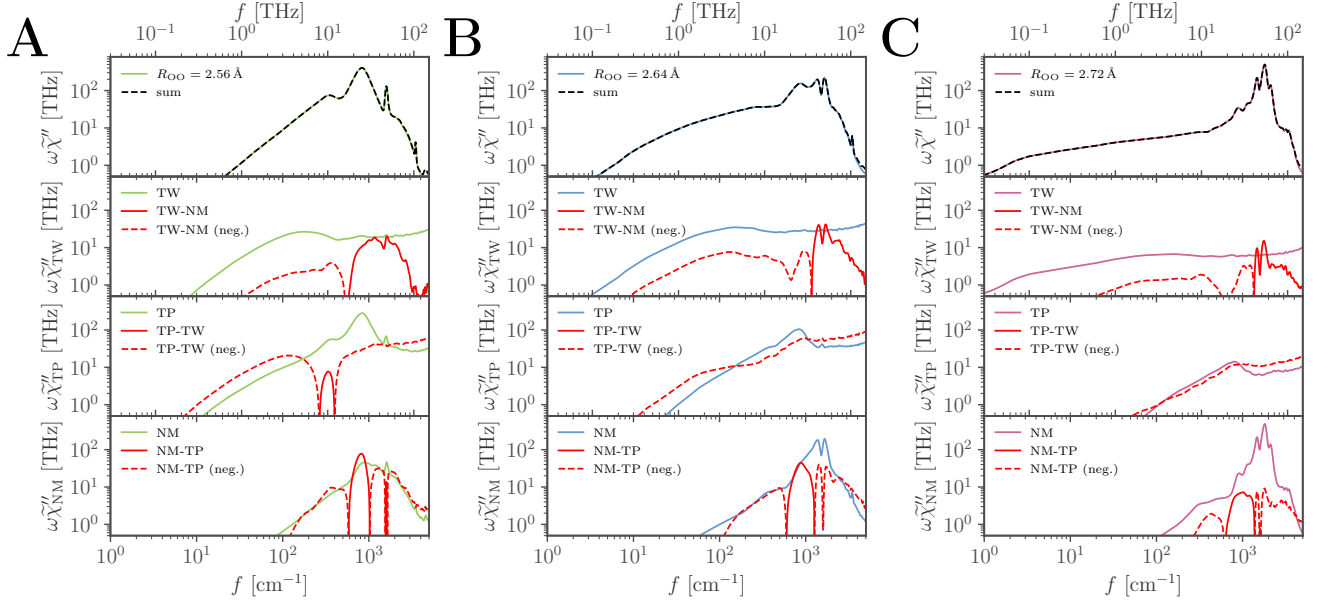


Figure S13. Spectral decomposition of the excess-proton dynamics in the  $\text{H}_5\text{O}_2^+$  cation for different constrained  $R_{\text{OO}}$  (**A**:  $R_{\text{OO}} = 2.56 \text{ \AA}$ , **B**:  $R_{\text{OO}} = 2.64 \text{ \AA}$ , **C**:  $R_{\text{OO}} = 2.72 \text{ \AA}$ ), similar to the results in fig. 2B in the main text (colored lines). The different cross-contributions are shown in red and negative cross-contributions as red broken lines.

## IX. DYNAMICS OF A TWO-STATE PROCESS

Consider an arbitrary two-state process  $d(t)$  characterized by a jump distance  $D$ , a jump-time probability distribution, which is the transfer-waiting-time probability distribution  $p_{\text{TW}}(t)$  with  $\int_0^\infty p_{\text{TW}}(t) dt = 1$ , and a survival probability  $q_{\text{TW}}(t) = \int_t^\infty p_{\text{TW}}(t') dt'$ . The conditional expectation values  $\langle d(t) \rangle_{d(0)}$  for the process starting at time  $t = 0$  at either  $d(0) = 0$  or  $d(0) = D$  are thus given as

$$\langle d(t) \rangle_{d(0)=0} = 0 p_{00}(t) + D p_{0D}(t), \quad (\text{S17})$$

$$\langle d(t) \rangle_{d(0)=D} = 0 p_{D0}(t) + D p_{DD}(t), \quad (\text{S18})$$

where  $p_{xy}(t)$  denotes the probability to be at  $d(t) = y$  when starting at  $d(0) = x$ . In the long-time limit each state has equal probability. The autocorrelation function,  $C(t) = \langle d(t)d(0) \rangle$ , is therefore given as

$$\langle d(t)d(0) \rangle = \frac{1}{2} (0 \langle d(t) \rangle_{d(0)=0} + D \langle d(t) \rangle_{d(0)=D}) \quad (\text{S19})$$

$$= \frac{D^2}{2} p_{DD}(t). \quad (\text{S20})$$

In order to express the probability  $p_{DD}(t)$  in terms of the first-passage-time distribution  $p_{\text{TW}}(t)$  and survival probability  $q_{\text{TW}}(t)$ , all possible jumps within time  $t$  have to be considered, as illustrated in fig. S14

$$p_{DD}(t) = \int_0^\infty dt_D q_{\text{TW}}(t_D) \sum_{N=0}^\infty \prod_{j=1}^N \int_0^\infty dt_j^D p_{\text{TW}}(t_j^D) \int_0^\infty dt_j^0 p_{\text{TW}}(t_j^0) \delta \left[ t - t_D - \sum_{j=1}^N (t_j^D + t_j^0) \right]. \quad (\text{S21})$$

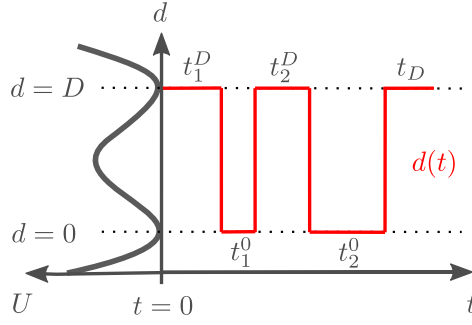


Figure S14. Schematic of a binary jump process  $d(t)$  with jumps separated by residence times  $t_j^0$  and  $t_j^D$  following the notation considered in eq.(S21). A doublewell potential,  $U(d)$ , is shown to highlight the relation of the binary jump process to the barrier-crossing dynamics.

Since  $p_{\text{TW}}(t)$  and  $q_{\text{TW}}(t)$  are single-sided, a single-sided Fourier transform is performed,

$$\begin{aligned} \tilde{p}_{\text{DD}}^+(\omega) &= \int_0^\infty dt e^{i\omega t} \int_0^\infty dt_D q_{\text{TW}}(t_D) \sum_{N=0}^\infty \prod_{j=1}^N \int_0^\infty dt_j^D p_{\text{TW}}(t_j^D) \\ &\quad \int_0^\infty dt_j^0 p_{\text{TW}}(t_j^0) \delta \left[ t - t_D - \sum_{j=1}^N (t_j^D + t_j^0) \right] \end{aligned} \quad (\text{S22})$$

$$= \int_0^\infty dt_D q_{\text{TW}}(t_D) \sum_{N=0}^\infty \prod_{j=1}^N \int_0^\infty dt_j^D p_{\text{TW}}(t_j^D) \quad (\text{S23})$$

$$\begin{aligned} &\int_0^\infty dt_j^0 p_{\text{TW}}(t_j^0) e^{i\omega [t_D + \sum_{j=1}^N (t_j^D + t_j^0)]} \\ &= \tilde{q}_{\text{TW}}(\omega) \sum_{N=0}^\infty \tilde{p}_{\text{TW}}(\omega)^{2N} \end{aligned} \quad (\text{S24})$$

$$= \frac{\tilde{q}_{\text{TW}}(\omega)}{1 - \tilde{p}_{\text{TW}}(\omega)^2}, \quad (\text{S25})$$

and it follows for the single-sided Fourier transformed autocorrelation

$$\tilde{C}^+(\omega) = \frac{D^2}{2} \frac{\tilde{q}_{\text{TW}}(\omega)}{1 - \tilde{p}_{\text{TW}}(\omega)^2}. \quad (\text{S26})$$

From eqs. (S10) and (S26) we obtain our expression for the response function of the binary jump process

$$\tilde{\chi}_{\text{DD}}(\omega) = -\frac{D^2}{2k_B T} \left( 1 - \frac{i\omega \tilde{q}_{\text{TW}}(\omega)}{1 - \tilde{p}_{\text{TW}}(\omega)^2} \right). \quad (\text{S27})$$

In case of the jumping variable  $d(t)$  being a polarization with polarization jump  $2qd_{\text{TW}}^*$ , where  $q$  is the charge, the dielectric susceptibility of the binary polarization jump process reads

$$\tilde{\chi}(\omega) = -\frac{2q^2 d_{\text{TW}}^{*2}}{V \epsilon_0 k_B T} \left( 1 - \frac{i\omega \tilde{q}_{\text{TW}}(\omega)}{1 - \tilde{p}_{\text{TW}}(\omega)^2} \right), \quad (\text{S28})$$

and eventually its power spectrum, proportional to the imaginary part of the dielectric susceptibility, is obtained as

$$\omega \tilde{\chi}''(\omega) = \frac{2q^2 d_{\text{TW}}^{*2}}{V \epsilon_0 k_B T} \text{Re} \left( \frac{\omega^2 \tilde{q}_{\text{TW}}(\omega)}{1 - \tilde{p}_{\text{TW}}(\omega)^2} \right). \quad (\text{S29})$$

## X. POWER SPECTRUM OF THE DAMPED HARMONIC OSCILLATOR

The absorbed power  $\omega\tilde{\chi}_{xx}''(\omega)$  of the damped harmonic oscillator described by the differential equation

$$m\ddot{x}(t) = -\gamma\dot{x}(t) - kx(t) + F_{\text{ext}}(t), \quad (\text{S30})$$

is computed from the linear response in Fourier space

$$\tilde{\chi}_{xx}(\omega) = \frac{\tilde{x}(\omega)}{\tilde{F}_{\text{ext}}(\omega)} \quad (\text{S31})$$

$$= (k - m\omega^2 - i\gamma\omega)^{-1} \quad (\text{S32})$$

$$= \frac{k - m\omega^2 + i\gamma\omega}{(k - m\omega^2)^2 + \gamma^2\omega^2}, \quad (\text{S33})$$

where  $\tilde{x}(\omega)$  is the oscillating variable,  $m$  the mass,  $\gamma$  the friction coefficient,  $k$  the spring constant of the harmonic potential and  $\tilde{F}_{\text{ext}}(\omega)$  an external force. For the power spectrum follows

$$\omega\tilde{\chi}_{xx}''(\omega) = \frac{\gamma\omega^2}{(k - m\omega^2)^2 + \gamma^2\omega^2}, \quad (\text{S34})$$

which by introducing the time scales  $\tau = 2\gamma/k$ ,  $\tau_m = \sqrt{m/k}$  and length scale  $D$  with  $D^2 = k_B T/k$  converts to

$$\omega\tilde{\chi}_{xx}''(\omega) = \frac{2D^2}{k_B T} \frac{\tau\omega^2}{4(1 - \tau_m^2\omega^2)^2 + \tau^2\omega^2}. \quad (\text{S35})$$

In case of the oscillating variable  $x(t)$  being a polarization with polarization jump  $qD$ , where  $q$  is the charge, the dielectric susceptibility reads

$$\omega\tilde{\chi}''(\omega) = \frac{2q^2 D^2}{V\epsilon_0 k_B T} \frac{\tau\omega^2}{4(1 - \tau_m^2\omega^2)^2 + \tau^2\omega^2}. \quad (\text{S36})$$

In spectroscopy this is known as a Lorentz band shape, which in the overdamped case,  $\tau_m \rightarrow 0$ , reads

$$\omega\tilde{\chi}''(\omega) = \frac{2q^2 D^2}{V\epsilon_0 k_B T} \frac{\tau\omega^2}{4 + \tau^2\omega^2}, \quad (\text{S37})$$

known as the Debye band shape [20].

## XI. TRANSFER-PATH SHAPE

Kim and Netz [21] derived the transfer-path-time shape  $t(d_{\text{TP}})$  over a harmonic barrier by an exact calculation, valid for arbitrary barrier height, as

$$t(d_{\text{TP}}) = \tau - \frac{2\gamma d_{\text{TW}}^{*2}}{k_B T U} \int_{\sqrt{U}}^{\sqrt{U}(d_{\text{TP}}/d_{\text{TW}}^*-1)} dy \left( \frac{\text{erf}(y) - \text{erf}(\sqrt{U})}{\text{erf}(\sqrt{U}(d_{\text{TP}}/d_{\text{TW}}^*-1)) - \text{erf}(\sqrt{U})} - \frac{1}{2} \right) D_+(y), \quad (\text{S38})$$

where  $D_+(x) = e^{-x^2} \int_0^x dt e^{t^2}$  is the Dawson integral function,  $\gamma$  is the friction constant,  $U = U_0/k_B T$  is the dimensionless barrier height,  $d_{\text{TW}}^*$  a length scale and  $\tau$  a time scale. Note that the shape function is given by time  $t$  as a function of position  $d$ . The second term in eq. (S38) vanishes for  $d_{\text{TP}} = 2d_{\text{TW}}^*$  and reduces to  $-\tau$  for  $d_{\text{TP}} = 0$  and therefore  $t(d_{\text{TP}} = 0) = 0$  and  $t(d_{\text{TP}} = 2d_{\text{TW}}^*) = \tau$ . For a variable  $s = y/\sqrt{U}$ , eq. (S38) is rewritten as

$$t(d_{\text{TP}}) = \tau - \frac{2\gamma d_{\text{TW}}^{*2}}{k_B T \sqrt{U}} \int_1^{d_{\text{TP}}/d_{\text{TW}}^*-1} ds \left( \frac{\text{erf}(\sqrt{U}s) - \text{erf}(\sqrt{U})}{\text{erf}(\sqrt{U}(d_{\text{TP}}/d_{\text{TW}}^*-1)) - \text{erf}(\sqrt{U})} - \frac{1}{2} \right) D_+(\sqrt{U}s), \quad (\text{S39})$$

For large  $U \gg 1$  and  $d_{\text{TW}}^* < d_{\text{TP}} < 2d_{\text{TW}}^*$ , eq. (S39) has an asymptotic expression

$$\begin{aligned} t(d_{\text{TP}}) &\approx \tau + \frac{\gamma d_{\text{TW}}^{*2}}{k_B T} \int_1^{d_{\text{TP}}/d_{\text{TW}}^*-1} dt \frac{D_+(\sqrt{U}t)}{\sqrt{U}} \\ &= \tau + \frac{\gamma d_{\text{TW}}^{*2}}{2k_B T U} \ln(d_{\text{TP}}/d_{\text{TW}}^* - 1), \end{aligned} \quad (\text{S40})$$

where we use  $D_+(\sqrt{U}t)/\sqrt{U} \approx 1/(2Us)$ .

Therefore, further using the symmetric nature of  $t(d_{\text{TP}})$  in the limit  $U \rightarrow \infty$ , we obtain the asymptotic expression for  $t(d_{\text{TP}})$  as

$$t(d_{\text{TP}}) = \begin{cases} -\frac{\gamma d_{\text{TW}}^{*2}}{2k_B T U} \ln(1 - d_{\text{TP}}/d_{\text{TW}}^*), & \text{for } 0 < d_{\text{TP}} < d_{\text{TW}}^* \\ \tau + \frac{\gamma d_{\text{TW}}^{*2}}{2k_B T U} \ln(d_{\text{TP}}/d_{\text{TW}}^* - 1), & \text{for } d_{\text{TW}}^* < d_{\text{TP}} < 2d_{\text{TW}}^*. \end{cases} \quad (\text{S41})$$

It is straightforward to solve eq. (S41) for  $d_{\text{TP}}$ , yielding

$$d_{\text{TP}}(t) = \begin{cases} -d_{\text{TW}}^* \left( e^{-\frac{2k_B T U t}{\gamma d_{\text{TW}}^{*2}}} - 1 \right), & \text{for } 0 < t < \tau/2 \\ d_{\text{TW}}^* \left( e^{\frac{2k_B T U (t-\tau)}{\gamma d_{\text{TW}}^{*2}}} + 1 \right), & \text{for } \tau/2 < t < \tau. \end{cases} \quad (\text{S42})$$

Using the curvature parameter  $\kappa = \gamma d_{\text{TW}}^{*2}/(2k_B T U)$ , and shifting the variables  $t \rightarrow t + \tau/2$  and  $d_{\text{TP}} \rightarrow d_{\text{TP}} + d_{\text{TW}}^*$  to fulfill  $d_{\text{TP}}(t = 0) = 0$ , we arrive at the leading order expression as the sum of the above two

$$\begin{aligned} d_{\text{TP}}(t) &= d_{\text{TW}}^* \left[ e^{-\frac{\tau-2t}{2\kappa}} - e^{-\frac{\tau+2t}{2\kappa}} \right] \\ &= d_{\text{TW}}^* \left[ e^{t/\kappa} - e^{-t/\kappa} \right] / e^{\frac{\tau}{2\kappa}}. \end{aligned} \quad (\text{S43})$$

This expression is easily compared to the transfer-path shape (in the presence of a harmonic potential) derived from the path-integral approach (equivalent to eq. 3 in the main text) [22, 23]

$$d_{\text{TP}}(t) = d_{\text{TW}}^* \left[ e^{t/\kappa} - e^{-t/\kappa} \right] / \mathcal{N}, \quad (\text{S44})$$

with a slightly different normalization factor  $\mathcal{N} = e^{\frac{\tau}{2\kappa}} - e^{-\frac{\tau}{2\kappa}}$ . Note that the difference vanishes in the high-barrier limit  $U \rightarrow \infty$ , i.e.  $\kappa \rightarrow 0$ , in which limit eq. (S43) derived from reference [21] becomes equivalent to eq. (S44) derived from the path-integral approach.

## XII. SPECTRAL SIGNATURES OF TRANSFER PATHS

The IR spectral signature of transfer paths is derived by modeling the Fourier-transformed transfer-path contribution  $\tilde{d}_{\text{TP}}(\omega)$  based on the transfer-path time  $\tau_{\text{TP}}$  and the recrossing-number probability distribution  $p_{\text{RN}}(n)$ . Recall that the power spectrum  $\omega\tilde{\chi}''(\omega)$  of a stochastic process  $x(t)$  limited to the time domain  $[0, L_t]$  is computed from the Fourier-transformed expressions  $\tilde{x}(\omega)$  as presented in section VII. In the following an expression for  $\tilde{d}_{\text{TP}}(\omega)$  is derived, based on the model for  $d_{\text{TP}}(t)$  illustrated in fig. S15A. The mean transfer path is expected to repeat on average with period  $\tau_{\text{TW}}$ . The model is therefore constrained to  $[0, \tau_{\text{TW}}]$  and using eq. (S13) the IR power spectrum of the transfer-path contribution can then be written as

$$\omega\tilde{\chi}''_{\text{TP}}(\omega) = \omega^2 \frac{q^2}{V\epsilon_0 k_B T \tau_{\text{TW}}} \tilde{d}_{\text{TP}}(\omega) \tilde{d}_{\text{TP}}^*(\omega). \quad (\text{S45})$$

$d_{\text{TP}}(t)$  is modeled by a single mean transfer path with shape  $d_{\text{TP}}^0(t)$  that is followed by a subsequent number of recrossing transfer paths, according to the recrossing-number probability distribution  $p_{\text{RN}}(n)$

$$d_{\text{TP}}(t) = \sum_{n=0}^{\infty} p_{\text{RN}}(n) \sum_{m=0}^n (-1)^m d_{\text{TP}}^0(t - m\tau_{\text{TP}}), \quad (\text{S46})$$

where the factor  $(-1)^m$  accounts for the alternation of recrossing transfer paths that are going up and down. A Fourier transform with respect to  $t$  turns the previous eq. (S46) into

$$\begin{aligned} \tilde{d}_{\text{TP}}(\omega) &= \sum_{n=0}^{\infty} p_{\text{RN}}(n) \sum_{m=0}^n (-1)^m \int_{-\infty}^{\infty} dt e^{i\omega t} d_{\text{TP}}^0(t - m\tau_{\text{TP}}) \\ &= \tilde{d}_{\text{TP}}^0(\omega) \sum_{n=0}^{\infty} p_{\text{RN}}(n) \sum_{m=0}^n (-1)^m e^{-i\omega m\tau_{\text{TP}}}. \end{aligned} \quad (\text{S47})$$

An expression for the mean transfer-path shape  $d_{\text{TP}}^0(t)$  is obtained by regarding the ensembles of rescaled transfer paths, which are shown in fig. S16 for various  $R_{\text{OO}}$ , along with the mean transfer paths, obtained from space-averaging the ensembles of rescaled transfer paths at each rescaled time between between the respective turning points of the trajectory. The mean value at the turning points defines the length scale  $d_{\text{TP}}^*$ . The single mean transfer path  $d_{\text{TP}}^0(t)$  reaching between the turning points is then modeled by a truncated straight line

$$d_{\text{TP}}^0(t) = 2d_{\text{TP}}^* \frac{t}{\tau_{\text{TP}}} (\theta(t) - \theta(t - \tau_{\text{TP}})), \quad (\text{S48})$$

with the Fourier transform

$$\tilde{d}_{\text{TP}}^0(\omega) = d_{\text{TP}}^* \frac{e^{i\omega\tau_{\text{TP}}} (2 - i\omega\tau_{\text{TP}}) - 2 - i\omega\tau_{\text{TP}}}{\omega^2 \tau_{\text{TP}}}. \quad (\text{S49})$$

The time scale  $\tau_{\text{TP}}$  in eq. (S47) is estimated directly from the simulation data, using the distributions, shown in fig. S15B – D. The distributions of transfer-path times considering only multiple transfers in fig. S15B–D are sharply peaked at roughly the same value for all systems  $\tau_{\text{TP}} = 0.023$  ps.

To account for subsequent recrossings, the expression eq. (S47) is evaluated for an exponential decay of the recrossing-number probability distribution,  $p_{\text{RN}}(n) = (1 - e^{-\alpha})e^{-\alpha n}$ , with decay parameter  $\alpha$  and shown in fig. S17 for the given systems. Using this fit function the final expression for the transfer-path spectral contribution evaluates to

$$\omega\tilde{\chi}''_{\text{TP}}(\omega) = \frac{2d_{\text{TP}}^*{}^2 q^2}{V\epsilon_0 k_B T \tau_{\text{TW}}} \frac{e^{\alpha} (\omega\tau_{\text{TP}} \cos(\frac{\omega\tau_{\text{TP}}}{2}) - 2 \sin(\frac{\omega\tau_{\text{TP}}}{2}))^2}{\omega^2 \tau_{\text{TP}}^2 (\cosh(\alpha) + \cos(\omega\tau_{\text{TP}}))}. \quad (\text{S50})$$

An approximate expression for eq. (S50) is derived by factorizing  $\omega\tilde{\chi}''_{\text{TP}}(\omega)$  into the recrossing contribution  $X_{\text{rec}}(\omega, \alpha, \tau_{\text{TP}})$  and the shape contribution  $|\tilde{d}_{\text{TP}}^0(\omega, \tau_{\text{TP}})|^2$

$$|\tilde{d}_{\text{TP}}^0(\omega, \tau_{\text{TP}})|^2 = d_{\text{TP}}^*{}^2 \frac{2^4 (\omega\tau_{\text{TP}} \cos(\frac{\omega\tau_{\text{TP}}}{2}) - 2 \sin(\frac{\omega\tau_{\text{TP}}}{2}))^2}{\omega^4 \tau_{\text{TP}}^2}, \quad (\text{S51})$$

$$X_{\text{rec}}(\omega, \alpha, \tau_{\text{TP}}) = \frac{e^{\alpha}}{2 (\cosh(\alpha) + \cos(\omega\tau_{\text{TP}}))}, \quad (\text{S52})$$

$$\omega\tilde{\chi}''_{\text{TP}}(\omega) = \frac{q^2 \omega^2}{V\epsilon_0 k_B T \tau_{\text{TW}}} X_{\text{rec}}(\omega, \alpha, \tau_{\text{TP}}) |\tilde{d}_{\text{TP}}^0(\omega, \tau_{\text{TP}})|^2. \quad (\text{S53})$$

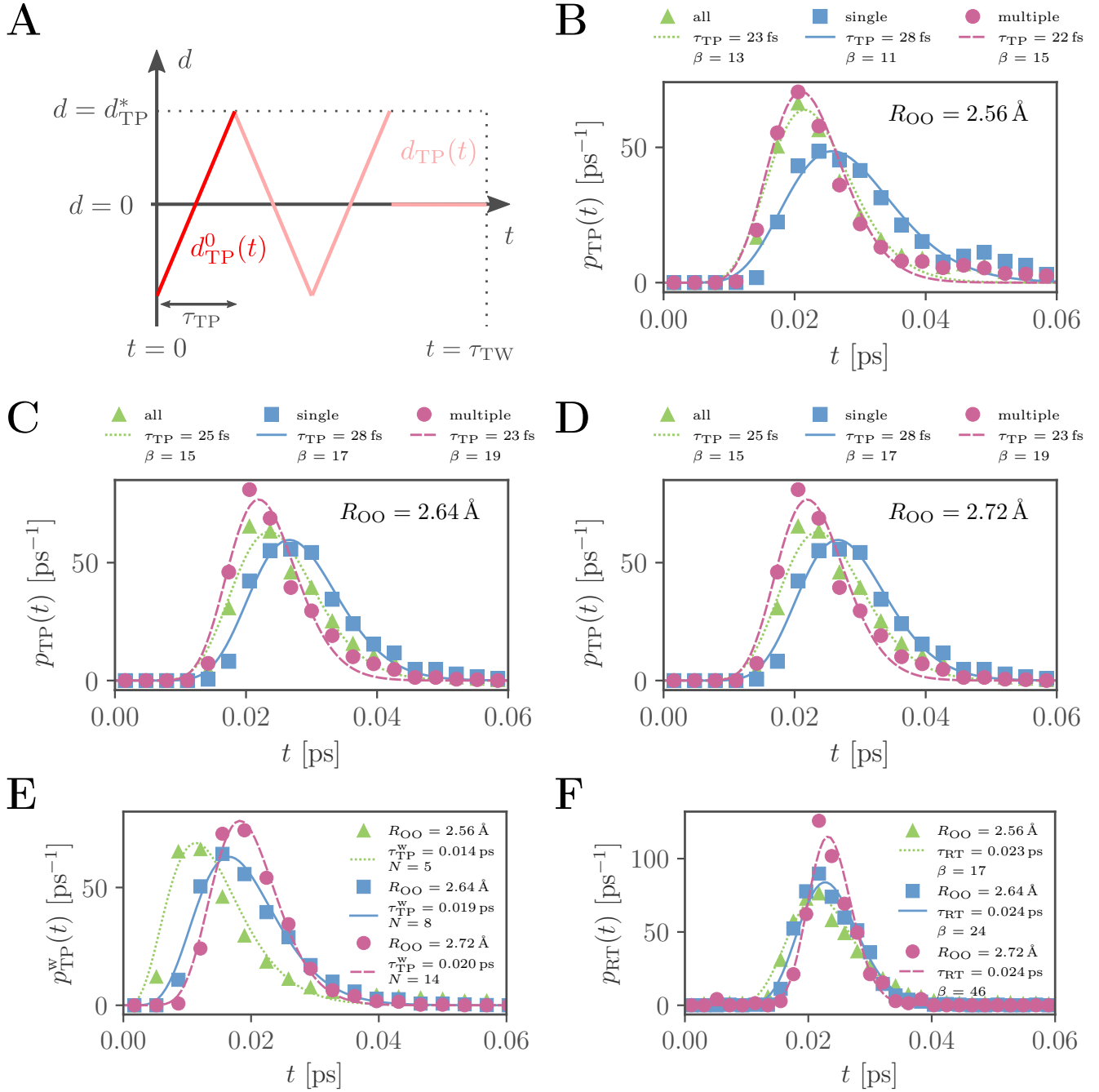


Figure S15. **A** Model for the transfer-path trajectory  $d_{\text{TP}}(t)$  with length  $\tau_{\text{TW}}$ . In this example the initial transfer path  $d_{\text{TP}}^0(t)$  with duration  $\tau_{\text{TP}}$  is centered around  $t = 0$  and followed by  $N = 2$  recrossing transfer paths, where  $N$  is drawn from the recrossing-number probability distribution  $p_{\text{RN}}(N)$ . The recrossing transfer paths are alternating and shifted relative to each other by the recrossing time  $\tau_{\text{RT}} \approx \tau_{\text{TP}}$ . **B–D** Transfer-path-time probability distributions measured between the turning points ( $p_{\text{TP}}(t)$ , B–D), between the minima of the free-energy landscape, ( $p_{\text{TP}}^{\text{w}}(t)$ , E) and recrossing-time distributions measured between recrossing of  $d = 0$  ( $p_{\text{RT}}(t)$ , F). The distributions (data points) are fitted to  $p_{\text{TP}}(t) = \frac{t^{\beta-1}}{(\beta-1)!} \left(\frac{\beta}{\tau}\right)^{\beta} e^{-\beta t/\tau}$  (solid, broken or dotted lines). Note that only the red curves in B–D are considered in the calculation of the TP spectral signature.

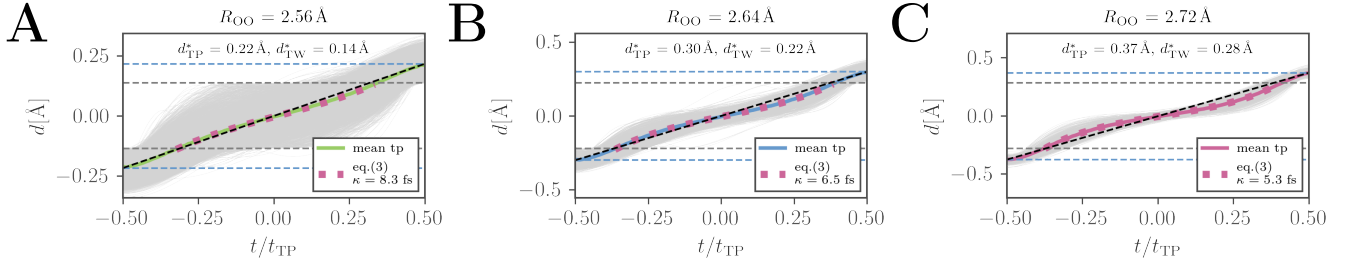


Figure S16. Ensembles of transfer paths sampled from the trajectories of the excess proton in the  $\text{H}_5\text{O}_2^+$  cation for different constrained oxygen distances  $R_{\text{OO}}$  (**A**:  $R_{\text{OO}} = 2.56 \text{ \AA}$ , **B**:  $R_{\text{OO}} = 2.64 \text{ \AA}$ , **C**:  $R_{\text{OO}} = 2.72 \text{ \AA}$ ), scaled to their individual transfer-path times  $t_{\text{TP}}$  between the respective turning points. The blue dashed lines indicate the mean initial and final values, which are used to estimate the parameter  $d_{\text{TP}}^*$ , the mean transfer-path distance along  $d$ . The horizontal black dashed lines indicate the minima of the free energy, which are used to estimate the parameter  $d_{\text{TW}}^*$ . Mean transfer paths between the minima of the free energy (colored lines) are fitted using eq. (3). The fits are shown as red dotted lines. Fit parameters are given in the legend.

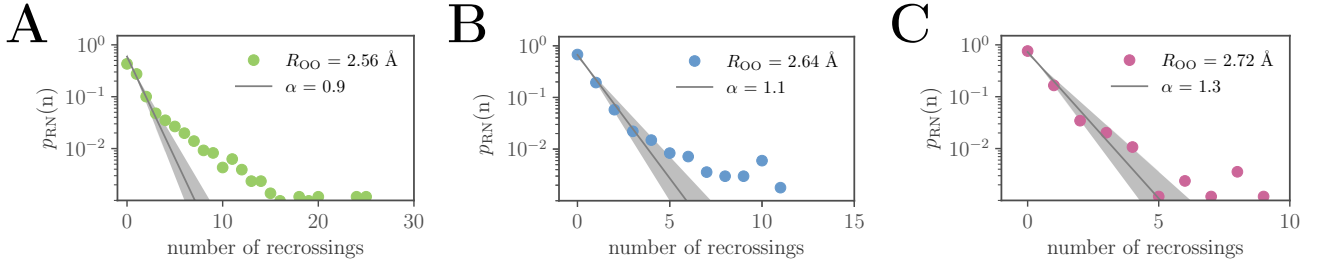


Figure S17. Recrossing-number probability distributions  $p_{\text{RN}}(n)$  for different constrained oxygen distances  $R_{\text{OO}}$  (**A**:  $R_{\text{OO}} = 2.56 \text{ \AA}$ , **B**:  $R_{\text{OO}} = 2.64 \text{ \AA}$ , **C**:  $R_{\text{OO}} = 2.72 \text{ \AA}$ ), normalized to  $\sum_{n=0}^{\infty} p_{\text{RN}} = 1$  and fits according to  $p_{\text{RN}}(n) = (1 - e^{-\alpha})e^{-\alpha n}$ . The grey shaded areas show the variation of  $\alpha \pm 20\%$

The relevant maximum of  $X_{\text{rec}}(\omega, \alpha, \tau_{\text{TP}})$  resides at  $\omega = \pi/\tau_{\text{TP}}$ , which minimizes the denominator in eq.(S52). A Taylor expansion of the cos function in eq.(S52) to second order in  $\omega$  around  $\pi/\tau_{\text{TP}}$  leads to

$$X_{\text{rec}}(\omega, \alpha, \tau_{\text{TP}}) = \frac{e^{\alpha}}{2 \cosh(\alpha) - 2 + (\omega\tau_{\text{TP}} - \pi)^2}. \quad (\text{S54})$$

Furthermore the shape contribution  $|\tilde{d}_{\text{TP}}^0(\omega, \tau_{\text{TP}})|^2$  can be estimated around  $\omega = \pi/\tau_{\text{TP}}$  by the following expression, which is in good agreement with the local series expansion

$$|\tilde{d}_{\text{TP}}^0(\omega, \tau_{\text{TP}})|^2 = d_{\text{TP}}^{*2} \frac{64\omega^2\tau_{\text{TP}}^4}{\pi^4(\omega\tau_{\text{TP}} + \pi)^2}, \quad (\text{S55})$$

$$\omega\tilde{\chi}_{\text{TP}}''(\omega) = \frac{d_{\text{TP}}^{*2}q^2}{V\epsilon_0k_B T\tau_{\text{TW}}} \frac{64e^{\alpha}\omega^4\tau_{\text{TP}}^4}{\pi^4(\omega\tau_{\text{TP}} + \pi)^2(2 \cosh(\alpha) - 2 + (\omega\tau_{\text{TP}} - \pi)^2)}. \quad (\text{S56})$$

Note that eq. (S56) is a multiplication of a function of Debye-shape type with the shoulder frequency at  $\omega = \pi/\tau_{\text{TP}}$ , stemming from the shape contribution eq. (S55) and a function of Lorentz-shape type with the resonant frequency at  $\omega = \pi/\tau_{\text{TP}}$ , stemming from the recrossing contribution eq. (S54).

If the transfer-path shape  $d_{\text{TP}}^0(t)$  is alternatively modeled by a truncated cosine wave with period  $2\tau_{\text{TP}}$

$$d_{\text{TP},\text{cos}}^0(t) = d_{\text{TP}}^* \cos\left(\frac{\pi t}{\tau_{\text{TP}}}\right) (\theta(t) - \theta(t - \tau_{\text{TP}})), \quad (\text{S57})$$

with the Fourier transform

$$\tilde{d}_{\text{TP},\text{cos}}^0(\omega) = -d_{\text{TP}}^* \frac{i\omega\tau_{\text{TP}}^2(1 + e^{i\omega\tau_{\text{TP}}})}{\omega^2\tau_{\text{TP}}^2 - \pi^2}, \quad (\text{S58})$$

a slightly different result is obtained.

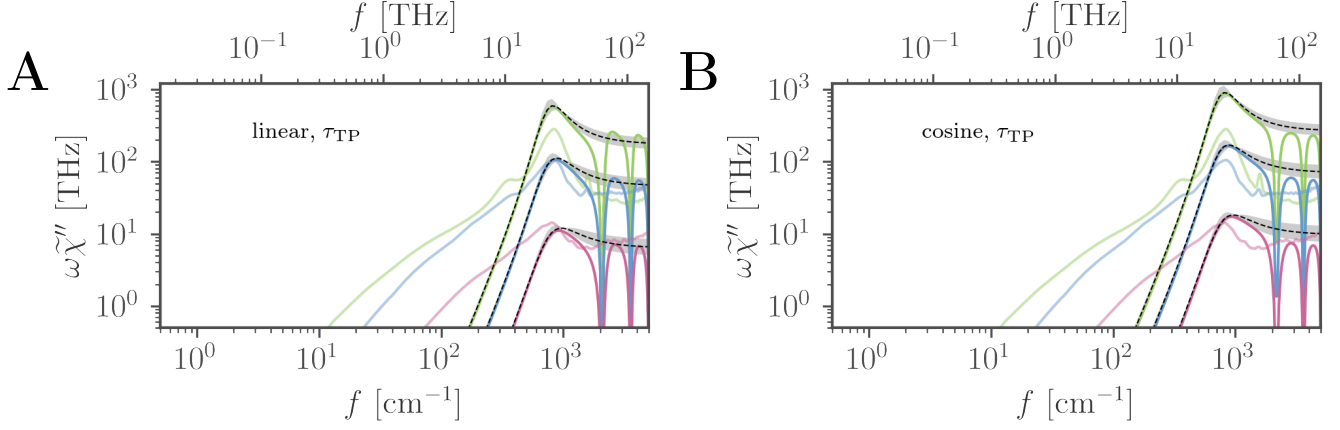


Figure S18. Models for the transfer-path spectral contribution given by eq. (S50) for the linear transfer-path shape (**A**) and eq. (S59) for the cosine transfer-path shape (**B**). The approximations are given by eqs. (S56) and (S60) and are shown as black dashed lines in A and B. The grey shaded areas show the variation of  $\alpha \pm 20\%$ .

The final expression

$$\omega \tilde{\chi}_{\text{TP,cos}}''(\omega) = \frac{d_{\text{TP}}^*{}^2 q^2}{V \epsilon_0 k_B T \tau_{\text{TW}}} \frac{e^\alpha \omega^4 \tau_{\text{TP}}^4 (\cos(\omega \tau_{\text{TP}}) + 1)}{(\pi^2 - \omega^2 \tau_{\text{TP}}^2)^2 (\cosh(\alpha) + \cos(\omega \tau_{\text{TP}}))}, \quad (\text{S59})$$

is Taylor-approximated as above to give

$$\omega \tilde{\chi}_{\text{TP,cos}}''(\omega) = \frac{d_{\text{TP}}^*{}^2 q^2}{V \epsilon_0 k_B T \tau_{\text{TW}}} \frac{e^\alpha \omega^4 \tau_{\text{TP}}^4}{(\omega \tau_{\text{TP}} + \pi)^2 (2 \cosh(\alpha) - 2 + (\omega \tau_{\text{TP}} - \pi)^2)}, \quad (\text{S60})$$

which are both shown in fig. S18B. In fact both approximate equations differ only by a factor of  $64/\pi^4 \approx 2/3$ . The linear shape was chosen for the presentation in the main text because of the good qualitative agreement of the mean TP shape in fig. S16 and quantitative agreement of the spectral shape in fig. S18A.



### XIII. IR SPECTRAL DECOMPOSITION OF THE EXCESS-PROTON DYNAMICS IN THE CONSTRAINED $\text{H}_5\text{O}_2^+$ CATION

Spectral decompositions of the excess-proton dynamics in the  $\text{H}_5\text{O}_2^+$  cation for different constrained  $R_{\text{OO}}$  are shown in fig. S19. Theoretical spectra are shown for the barrier-crossing model derived in section IX (respective eq. (1) in the main text) and the transfer-path model derived in section XII (respective eq. (5) in the main text), using the distance between the minima of the free energy in fig. 4B in the main text and fits applied to the distributions in fig. 4C in the main text and in section XII.

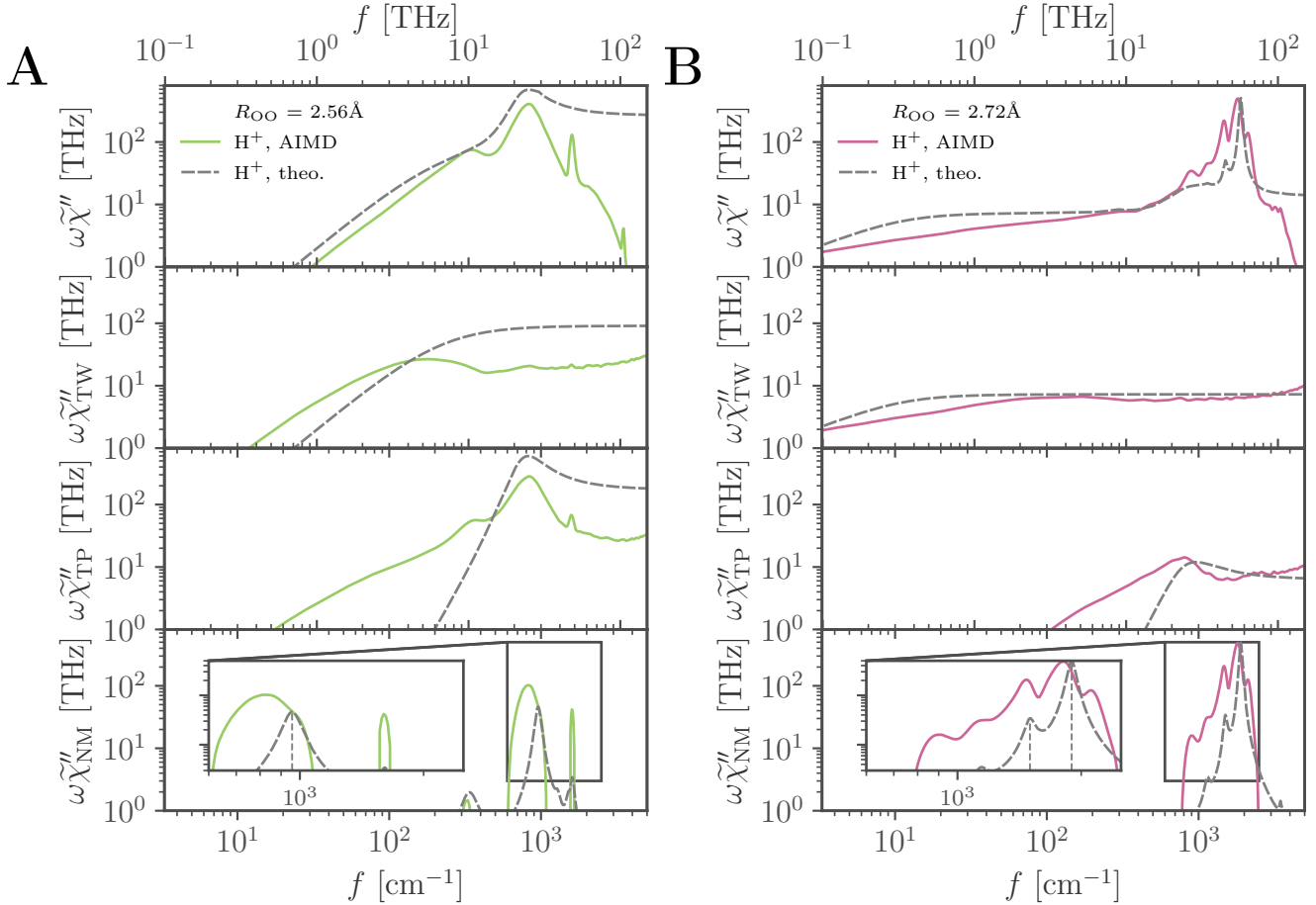


Figure S19. Spectral decomposition of the excess-proton dynamics in the  $\text{H}_5\text{O}_2^+$  cation for different constrained  $R_{\text{OO}}$  (**A**:  $R_{\text{OO}} = 2.56 \text{ \AA}$ , **B**:  $R_{\text{OO}} = 2.72 \text{ \AA}$ ) in analogy to the results in fig. 2B in the main text (colored lines). Theoretical spectra for the models discussed in the previous sections are shown as grey broken lines.

### XIV. IR SPECTRA OF THE DEUTERATED $\text{H}_5\text{O}_2^+$ CATION

In order to test isotope effects, simulations were performed with the excess proton replaced by an excess deuteron. The resulting IR spectra for various  $R_{\text{OO}}$  and directions are shown in fig. S20 and compared to the excess-proton data. The regime between  $400 \text{ cm}^{-1}$  to  $2000 \text{ cm}^{-1}$  shows various shifts to lower frequencies and also splittings. This H/D isotope effect is expected since this region is linked to the excess-proton motion. As expected, the OH-stretching vibrations are not effected. These vibrations are associated with the flanking water molecules, that are not deuterated. Fig. S21 compares the H/D isotope effect for the decomposed spectra. In contrast to the normal-modes involving the excess-proton as well as the transfer-path signature, which are all shifted by deuteration, the low-frequency transfer-waiting shoulder does not shift.

## XV. DEUTERON TRANSFER-WAITING RATES

As discussed in the previous section, no isotope effect is found for the low-frequency transfer-waiting shoulder of the IR spectrum, i.e. the mean transfer-waiting time  $\tau_{\text{TW}}$  does not depend on the mass of the reaction coordinate, but solely on friction constant  $\gamma$ . This is expected to be the same for the system with either an excess proton or an excess deuteron. The determination of the friction constant  $\gamma$  is not straight-forward. In fig. S22 the mean transfer-waiting times  $\tau_{\text{TW}}$  measured from the simulations are compared to the heuristic formula [24]

$$\tau_{\text{TW}} = e^{\frac{U_0}{k_B T}} \left[ \frac{m k_B T}{\gamma U_0} + \frac{\pi}{2\sqrt{2}} \frac{\gamma d_{\text{TW}}^*{}^2}{U_0} + 2\sqrt{\frac{m d_{\text{TW}}^*{}^2}{U_0}} \right]. \quad (\text{S61})$$

Since the mass  $m$ , barrier height  $U_0$  and widths of the barrier  $2d_{\text{TW}}^*$  are known (given in fig. S22), estimates for the friction constant  $\gamma$  are obtained by comparing the simulation data to the heuristic formula. The obtained values,  $\gamma \approx 400$  u/ps for  $R_{\text{OO}} = 2.64$  Å and  $\gamma \approx 900$  u/ps for  $R_{\text{OO}} = 2.72$  Å, vary greatly and also deviate from the friction constants fitted to the line-broadening of the normal-modes,  $\gamma = 16$  u/ps. This discrepancy highlights the complex frequency dependence of dielectric friction, as previously discussed by Sedlmeier et al. [25], Brünig et al. [26]. Note that the theoretical predictions are only valid for  $U_0 > 2k_B T$ , and can therefore not be used for interpretation of the data for the lowest barrier considered here [24]. Nevertheless, fig. S22 validates the observation of the negligible isotope effect on the mean transfer-waiting time, since the heuristic formula of eq. (S61) shows little mass dependence in the

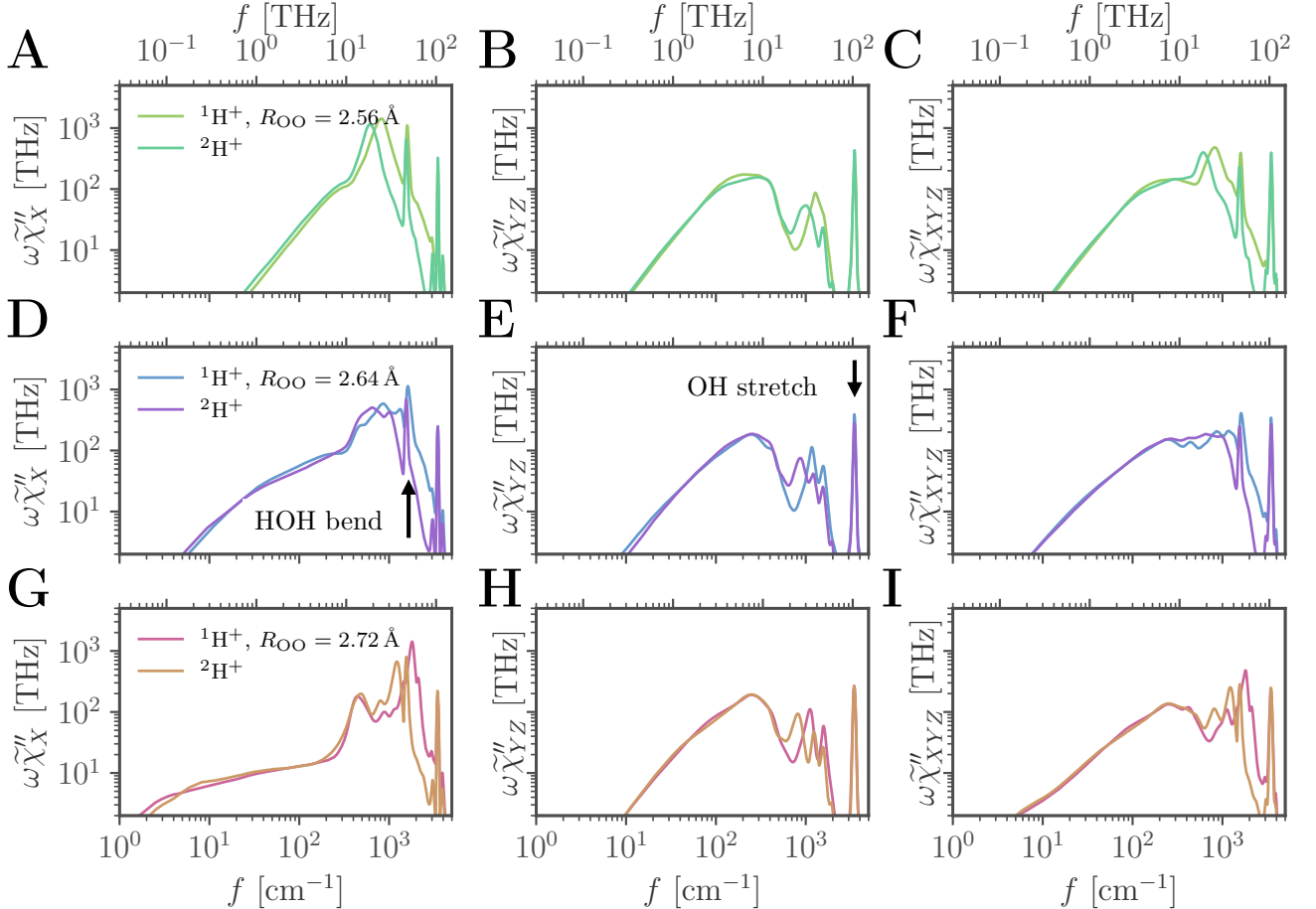


Figure S20. Comparison of the IR spectra of the  $\text{H}_5\text{O}_2^+$  cation with an excess proton ( $^1\text{H}^+$ ) or an excess deuteron ( $^2\text{H}^+$ ) in different directions **A**, **D**, **G**: along the  $x$ -axis connecting the two oxygens, **B**, **E**, **H**: along the  $yz$ -plane **C**, **F**, **I**: isotropic spectrum. Each row corresponds to a system with a distinct constrained oxygen distance  $R_{\text{OO}}$  given in the first legend. The HOH-bending mode and OH-stretching mode of the water molecules are indicated in **D** and **E**.

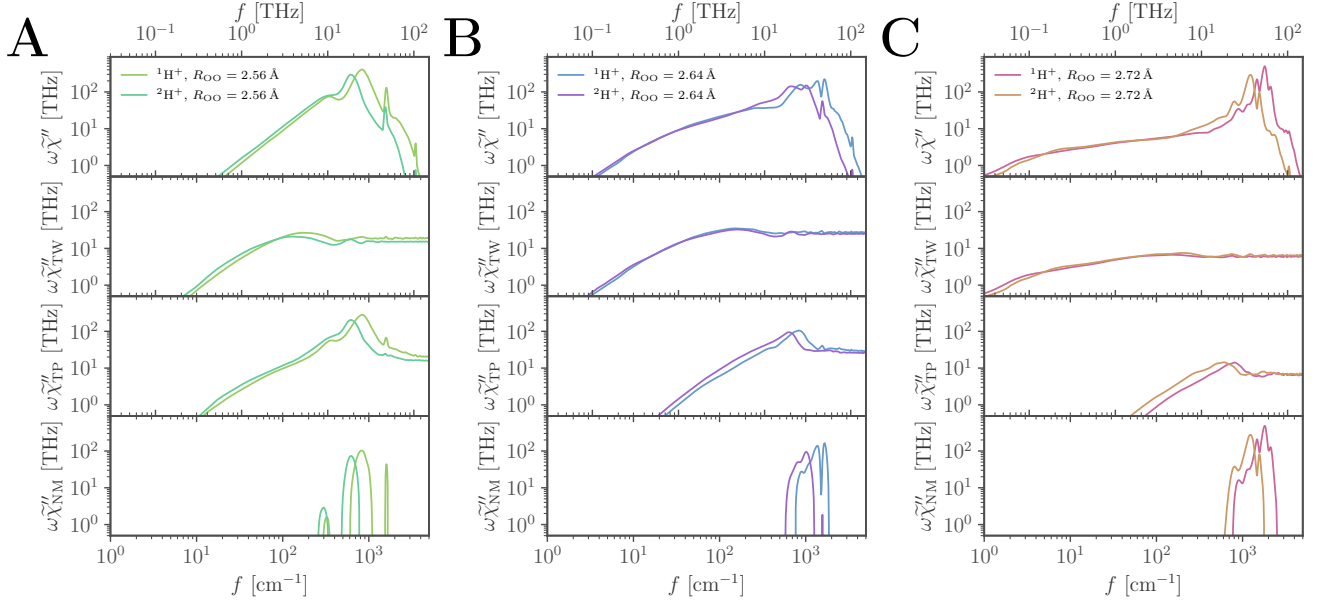


Figure S21. Comparison of the IR spectra of the  $\text{H}_5\text{O}_2^+$  cation with an excess proton ( $^1\text{H}^+$ ) or an excess deuteron ( $^2\text{H}^+$ ) for different  $R_{\text{OO}}$  (**A**:  $R_{\text{OO}} = 2.56 \text{ \AA}$ , **B**:  $R_{\text{OO}} = 2.64 \text{ \AA}$ , **C**:  $R_{\text{OO}} = 2.72 \text{ \AA}$ ), decomposed as described in the main text.

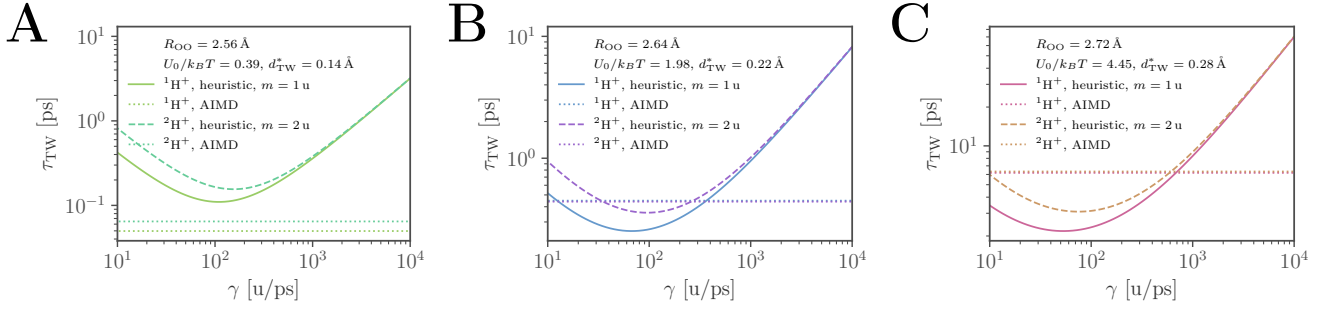


Figure S22. The transfer-waiting times  $\tau_{\text{TW}}$  of the excess proton ( $^1\text{H}^+$ ) and the excess deuteron ( $^2\text{H}^+$ ) of the  $\text{H}_5\text{O}_2^+$  cation for different constrained oxygen distances  $R_{\text{OO}}$  (dotted lines, **A**:  $R_{\text{OO}} = 2.56 \text{ \AA}$ , **B**:  $R_{\text{OO}} = 2.64 \text{ \AA}$ , **C**:  $R_{\text{OO}} = 2.72 \text{ \AA}$ ) compared to the heuristic formula, given by eq. (S61), (straight and broken lines) as a function of the friction constant  $\gamma$ . Parameters entering the heuristic formula are given in the legends.

predicted regime of  $\gamma$ , as seen in figs. S22B and S22C from the negligible difference between the curves for  $m = 1 \text{ u}$  (solid lines) and  $m = 2 \text{ u}$  (dashed lines) in the regime of the measured mean transfer-waiting time (dotted lines).

## XVI. WIENER-KINTCHINE THEOREM

The correlation function  $C_{xy}(t)$  of two stochastic processes  $x(t)$  and  $y(t)$  limited to the interval  $[0, L_t]$  is efficiently computed from the Fourier-transformed expressions  $\tilde{x}(\omega)$  and  $\tilde{y}(\omega)$  according to

$$C_{xy}(t) = \frac{1}{2\pi(L_t - t)} \int_{-\infty}^{\infty} d\omega e^{-i\omega t} \tilde{x}(\omega) \tilde{y}^*(\omega), \quad (\text{S62})$$

where the asterix denotes the conjugate form. This is known as the Wiener-Kintchine theorem [27]. Both sides of eq. (S62) are Fourier-transformed to give

$$\int_{-\infty}^{\infty} dt e^{i\omega t} L_t \left(1 - \frac{t}{L_t}\right) C_{xy}(t) = \tilde{x}(\omega) \tilde{y}^*(\omega), \quad (\text{S63})$$

which in the limit of large  $L_t$  reduces to

$$\tilde{C}_{xy}(\omega) = L_t^{-1} \tilde{x}(\omega) \tilde{y}^*(\omega). \quad (\text{S64})$$

Eq. (S62) can be derived starting off with the definition of the correlation function

$$C_{xy}(t) = \frac{1}{L_t - t} \int_0^{L_t - t} dt' x(t' + t) y(t'). \quad (\text{S65})$$

Defining  $x(t), y(t) = 0$  for  $t \notin [0, L_t]$ , the integral bounds can formally be extended

$$C_{xy}(t) = \frac{1}{L_t - t} \int_{-\infty}^{\infty} dt' x(t' + t) y(t'), \quad (\text{S66})$$

and making use of the convolution theorem

$$\begin{aligned} C_{xy}(t) &= \frac{1}{4\pi^2(L_t - t)} \int_{-\infty}^{\infty} dt' \int_{-\infty}^{\infty} d\omega e^{-i\omega(t+t')} \tilde{x}(\omega) \int_{-\infty}^{\infty} d\omega' e^{-i\omega't'} \tilde{y}(\omega') \\ &= \frac{1}{4\pi^2(L_t - t)} \int_{-\infty}^{\infty} d\omega e^{-i\omega t} \tilde{x}(\omega) \int_{-\infty}^{\infty} d\omega' \tilde{y}(\omega') \int_{-\infty}^{\infty} dt' e^{-it'(\omega+\omega')} \\ &= \frac{1}{4\pi^2(L_t - t)} \int_{-\infty}^{\infty} d\omega e^{-i\omega t} \tilde{x}(\omega) \int_{-\infty}^{\infty} d\omega' \tilde{y}(\omega') 2\pi\delta(\omega + \omega') \\ &= \frac{1}{2\pi(L_t - t)} \int_{-\infty}^{\infty} d\omega e^{-i\omega t} \tilde{x}(\omega) \tilde{y}(-\omega), \end{aligned} \quad (\text{S67})$$

noting that  $\tilde{y}(-\omega) = \tilde{y}^*(\omega)$  for a real function  $y(t)$  in order to obtain eq. (S62).

- 
- [1] Asmis, K. R. *et al.* Gas-Phase Infrared Spectrum of the Protonated Water Dimer. *Science* **299**, 1375 (2003).
  - [2] Fridgen, T. D., McMahon, T. B., MacAleese, L., Lemaire, J. & Maitre, P. Infrared spectrum of the protonated water dimer in the gas phase. *J. Phys. Chem. A* **108**, 9008 (2004).
  - [3] Diken, E. G. *et al.* Fundamental excitations of the shared proton in the  $\text{H}_3\text{O}_2^-$  and  $\text{H}_5\text{O}_2^+$  complexes. *J. Phys. Chem. A* **109**, 1487 (2005).
  - [4] Hammer, N. I. *et al.* The vibrational predissociation spectra of the  $\text{H}_5\text{O}_2^+ \cdot \text{RG}_n$  ( $\text{RG}=\text{Ar, Ne}$ ) clusters: Correlation of the solvent perturbations in the free OH and shared proton transitions of the Zundel ion. *J. Chem. Phys.* **122**, 244301 (2005).
  - [5] Dahms, F., Fingerhut, B. P., Nibbering, E. T., Pines, E. & Elsaesser, T. Large-amplitude transfer motion of hydrated excess protons mapped by ultrafast 2D IR spectroscopy. *Science* **357**, 491 (2017).
  - [6] Sauer, J. & Döbler, J. Gas-phase infrared spectrum of the protonated water dimer: Molecular dynamics simulation and accuracy of the potential energy surface. *ChemPhysChem* **6**, 1706 (2005).
  - [7] Vendrell, O., Gatti, F. & Meyer, H. D. Full dimensional (15-dimensional) quantum-dynamical simulation of the protonated water dimer. II. Infrared spectrum and vibrational dynamics. *J. Chem. Phys.* **127**, 184303 (2007).
  - [8] Park, M., Shin, I., Singh, N. J. & Kim, K. S. Eigen and Zundel forms of small protonated water clusters: Structures and infrared spectra. *J. Phys. Chem. A* **111**, 10692 (2007).

- [9] Kaledin, M., Kaledin, A. L., Bowman, J. M., Ding, J. & Jordan, K. D. Calculation of the vibrational spectra of  $\text{H}_5\text{O}_2^+$  and its deuterium-substituted isotopologues by molecular dynamics simulations. *J. Phys. Chem. A* **113**, 7671 (2009).
- [10] Huang, X., Braams, B. J. & Bowman, J. M. Ab initio potential energy and dipole moment surfaces for  $\text{H}_5\text{O}_2^+$ . *J. Chem. Phys.* **122**, 044308 (2005).
- [11] Baer, M., Marx, D. & Mathias, G. Theoretical messenger spectroscopy of microsolvated hydronium and Zundel cations. *Angew. Chemie - Int. Ed.* **49**, 7346 (2010).
- [12] Agostini, F., Vuilleumier, R. & Ciccotti, G. Infrared spectroscopy of small protonated water clusters at room temperature: An effective modes analysis. *J. Chem. Phys.* **134**, 084302 (2011).
- [13] Kulig, W. & Agmon, N. A 'clusters-in-liquid' method for calculating infrared spectra identifies the proton-transfer mode in acidic aqueous solutions. *Nat. Chem.* **5**, 29 (2013).
- [14] Rossi, M., Ceriotti, M. & Manolopoulos, D. E. How to remove the spurious resonances from ring polymer molecular dynamics. *J. Chem. Phys.* **140**, 234116 (2014).
- [15] Biswas, R., Carpenter, W., Fournier, J. A., Voth, G. A. & Tokmakoff, A. IR spectral assignments for the hydrated excess proton in liquid water. *J. Chem. Phys.* **146**, 154507 (2017).
- [16] Headrick, J. M., Bopp, J. C. & Johnson, M. A. Predissociation spectroscopy of the argon-solvated  $\text{H}_5\text{O}_2^+$  "zundel" cation in the 1000-1900  $\text{cm}^{-1}$  region. *J. Chem. Phys.* **121**, 11523 (2004).
- [17] Thämer, M., De Marco, L., Ramasesha, K., Mandal, A. & Tokmakoff, A. Ultrafast 2D IR spectroscopy of the excess proton in liquid water. *Science* **350**, 78 (2015).
- [18] Fournier, J. A., Carpenter, W. B., Lewis, N. H. & Tokmakoff, A. Broadband 2D IR spectroscopy reveals dominant asymmetric  $\text{H}_5\text{O}_2^+$  proton hydration structures in acid solutions. *Nat. Chem.* **10**, 932 (2018).
- [19] Wolke, C. T. *et al.* Spectroscopic snapshots of the proton-transfer mechanism in water. *Science* **354**, 1131 (2016).
- [20] Debye, P., *Polar Molecules* (Chemical Catalog Company, Incorporated, 1929).
- [21] Kim, W. K. & Netz, R. R. The mean shape of transition and first-passage paths. *J. Chem. Phys.* **143**, 224108 (2015).
- [22] Faccioli, P., Sega, M., Pederiva, F. & Orland, H. Dominant pathways in protein folding. *Phys. Rev. Lett.* **97**, 108101 (2006).
- [23] Cossio, P., Hummer, G. & Szabo, A. Transition paths in single-molecule force spectroscopy. *J. Chem. Phys.* **148**, 123309 (2018).
- [24] Kappler, J., Hinrichsen, V. B. & Netz, R. R. Non-Markovian barrier crossing with two-time-scale memory is dominated by the faster memory component. *Eur. Phys. J. E* **42**, 119 (2019).
- [25] Sedlmeier, F., Shadkhoo, S., Bruinsma, R. & Netz, R. R. Charge/mass dynamic structure factors of water and applications to dielectric friction and electroacoustic conversion. *J. Chem. Phys.* **140**, 054512 (2014).
- [26] Brünig, F. N., Geburtig, O., von Canal, A., Kappler, J. & Netz, R. R. Time-Dependent Friction Effects on Vibrational Infrared Frequencies and Line Shapes of Liquid Water. *J. Phys. Chem. B* **126**, 1579 (2022).
- [27] Wiener, N. Generalized harmonic analysis. *Acta Math.* **55**, 117 (1930).